Static or breakloose friction for lubricated contacts: the role of surface roughness and dewetting

2013 J. Phys.: Condens. Matter 25 445013

(http://iopscience.iop.org/0953-8984/25/44/445013)

J. Phys.: Condens. Matter **25** (2013) 445013 (22pp) doi:10.1088/0953-8984/25/44/445013

Static or breakloose friction for lubricated contacts: the role of surface roughness and dewetting

B Lorenz[1,5], B A Krick[2], N Rodriguez[3], W G Sawyer[2], P Mangiagalli[4] and B N J Persson[1,5]

[1] PGI, FZ-Jülich, D-52425 Jülich, Germany
[2] Department of Mechanical and Aerospace Engineering, University of Florida, Gainesville, FL 32611, USA
[3] Advanced Technologies, BD Medical-Pharmaceutical Systems, 1 Becton Drive, MC 427, Franklin Lakes, NJ 07417, USA
[4] Advanced Technologies, BD-Pharmaceutical Systems, F-38800 Pont de Claix, France

E-mail: b.persson@fz-juelich.de

Received 20 August 2013, in final form 18 September 2013
Published 16 October 2013
Online at stacks.iop.org/JPhysCM/25/445013

Abstract
We present experimental data for the static or breakloose friction for lubricated elastomer contacts, as a function of the time of stationary contact. Due to fluid squeeze-out from the asperity contact regions, the breakloose friction force increases continuously with the time of stationary contact. We consider three different cases: (a) PDMS rubber balls against flat smooth glass surfaces, (b) PDMS cylinder ribs against different substrates (glass, smooth and rough PMMA and an inert polymer) and (c) application to syringes. Due to differences in the surface roughness and contact pressures the three systems exhibit very different time dependences of the breakloose friction. In case (a) for rough surfaces the dry contact area A is a small fraction of the nominal contact area A_0, and the fluid squeeze-out is fast. In case (b) the dry contact area is close to the nominal contact area, $A/A_0 \approx 1$, and fluid squeeze-out is very slow due to percolation of the contact area. In this case, remarkably, different fluids with very different viscosities, ranging from 0.005 Pa s (water–glycerol mixture) to 1.48 Pa s (glycerol), give very similar breakloose friction forces as a function of the time of stationary contact. In case (c) the contact pressure and the surface roughness are larger than in case (b), and the squeeze-out is very slow so that even after a very long time the area of real contact is below the percolation threshold. For all cases (a)–(c), the increase in the breakloose friction is mainly due to the increase in the area of real contact with increasing time, because of the fluid squeeze-out and dewetting.

(Some figures may appear in colour only in the online journal)

1. Introduction

A non-zero force is usually necessary in order to slide a solid object on another solid object, e.g., a rectangular block on a (nominally) flat substrate. The static friction force F_s is the force necessary to initiate the sliding motion, while the kinetic friction force F_k is the force necessary to slide the block at a given (constant) velocity (here we assume that stick–slip motion does not occur). If F_N is the normal force the block exerts on the substrate, then the static friction coefficient $\mu_s = F_s/F_N$ and the kinetic friction coefficient $\mu_k = F_k/F_N$. While the kinetic friction coefficient often is a well defined quantity—which, however, depends on the material, surface condition (e.g., contamination films sliding velocity, temperature, humidity, ...)—the static friction coefficient depends on the history of the contact [1–3] (e.g., on the time of stationary contact) and also on the geometrical and

[5] www.MultiscaleConsulting.com.

elastic properties of the solids [4–7], and on how and where the external forces which induce the sliding are applied [8].

One particularly important origin of a time-dependent breakloose friction is fluid squeeze-out. That is, if two solid objects are squeezed together in a fluid, it will take time for the fluid to be removed from the asperity contact regions, and the breakloose friction force will increase with the time of stationary contact. As long as the fluid film thickness is larger than ∼10 nm the fluid squeeze-out depends on the bulk fluid viscosity η and one therefore expects a breakloose friction force which depends on η. Fluid squeeze-out is of extreme importance in many applications, e.g., for a tire on a wet road surface [9, 10], or for syringes (involving silicone oil squeeze-out between the rubber stopper and the lubricated barrel) [11].

In this paper we present experimental data for the static or breakloose friction for lubricated elastomer contacts, as a function of the time of stationary contact. Because of fluid squeeze-out from the asperity contact regions, the breakloose friction force increases continuously with the time of stationary contact. We consider three different cases: (a) PDMS rubber balls against glass surfaces, (b) PDMS cylinder ribs against different substrates (glass, smooth and rough PMMA and an inert polymer) and (c) application to syringes. Due to differences in the surface roughness and contact pressures the three systems exhibit very different time dependences of the breakloose friction. When the final (long contact time) contact area $A/A_0 \ll 1$, as is the case when the surface roughness is high enough and the nominal contact pressure small enough (as in the first system (a)), then many large flow channels percolate and the fluid can quickly escape without building up a large fluid pressure in the flow channels. In this case the fluid removal (both squeeze-out and dewetting) will occur fast. However, if $A/A_0 > 0.42$ at some point in time, as observed if the surfaces are smooth enough and the nominal contact pressure large enough (as for the second system (b)), the contact area will percolate, which may drastically slow down the squeeze-out, and also the dewetting process may be strongly affected as no percolating fluid flow channels will prevail at long contact times. No theory exists at present that can describe squeeze-out and dewetting simultaneously for randomly rough surfaces, but we believe that including dewetting will result in a contact area which will grow beyond the percolation limit. However, remarkably, different fluids with very different viscosities, ranging from 0.005 Pa s (water–glycerol mixture) to 1.48 Pa s (glycerol), give very similar breakloose friction forces as a function of the time of stationary contact. The increase in the breakloose friction is mainly due to the increase in the area of real contact with increasing contact time due to fluid squeeze-out and dewetting, but may involve additional physical processes in order to explain the similar squeeze-out times for fluids with very different viscosities. The application to syringes (case (c)) is similar to case (b), but involves higher applied nominal stress and larger surface roughness, and the squeeze-out is very slow, so that even after a very long time the area of real contact is below the percolation threshold. For all cases (a)–(c), the increase in the breakloose friction is mainly due to the increase in the area of real contact with increasing time, because of fluid squeeze-out and dewetting.

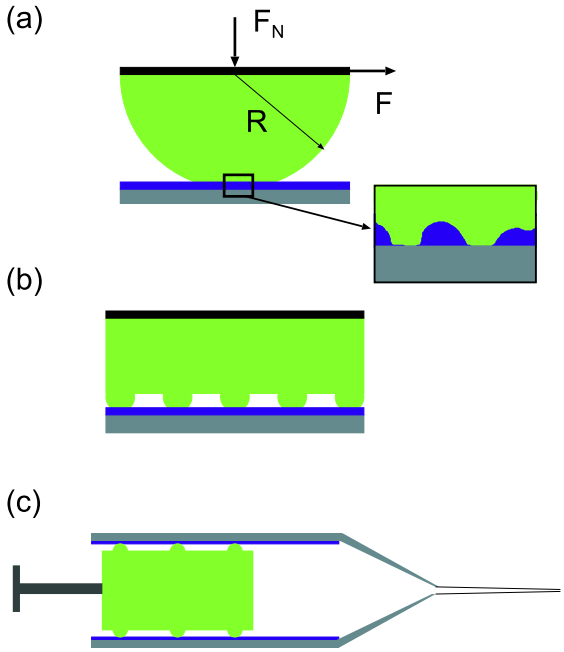

Figure 1. Experimental set-up used to study the breakloose friction. (a) PDMS ball squeezed against a nominally flat and lubricated surface. Due to surface roughness on the rubber ball the area of real contact between the rubber ball and the glass substrate is incomplete even after a long contact time. (b) PDMS block with ribs squeezed against a nominally flat and lubricated surface. (c) Syringe where the rubber stopper has ribs in contact with the lubricated barrel.

2. Experimental details

We have measured the dependence of the breakloose friction force on the time of stationary contact for three different systems (a)–(c), see figure 1. In the first experiment (a) (at the University of Florida), an optical *in situ* microtribometer [12, 13] was used to perform friction experiments between a PDMS half-sphere and a smooth glass surface (see figure 1(a)). The PDMS rubber hemispheres (radius $R =$ 1.5 mm) were produced by cross-linking transparent Sylgard 10:1 PDMS in an aluminum mold. The aluminum plate had a hemispherical hole that was sandblasted. The rough PDMS hemispheres were slid against a smooth glass countersample. The sphere is fixed to the end of a cantilever force transducer with its deflection monitored by capacitance probes. Optical images of the contact are processed to calculate the real contact area and the radius of the nominal (Hertzian) contact area.

The elastic modulus of the 10:1 crosslinked PDMS is $E \approx 2.2$ MPa. The experiments were performed with the load or normal force $F_N = 0.033$–0.058 N, giving the average Hertzian contact pressures $\sigma_N = 0.19$–0.23 MPa and (nominal) contact radius $r_0 = 0.23$–0.28 mm. Experiments were performed for dry contact and for interfaces lubricated by water (viscosity $\eta = 0.001$ Pa s) and silicone oil (viscosity $\eta = 1$ Pa s). The start-up (or breakloose) drive velocity was 0.1 mm s^{-1} in most of the experiments.

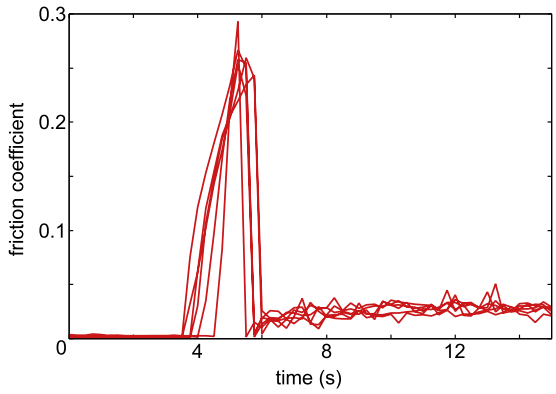

Figure 2. The friction force as a function of time after a 10 min squeeze-out time. For smooth PMMA lubricated with silicone oil (viscosity $\eta = 1$ Pa s). The drive velocity $v \approx 1$ mm s^{-1}.

The experimental set-up for the second type of experiments (b) (performed in the Jülich lab) is shown in figure 1(b) and described in more detail in [7]. We have produced a block with semicircular profiles (cylindrical ribs) on its lower surface, which are squeezed against a lubricated substrate. The block is made from PDMS rubber crosslinked in a steel mold. The negative of the ribs (i.e., the mold) was made using spark erosion, followed by electropolishing, which produces randomly rough surfaces having a roughness with nearly isotropic properties (see section 4.1). The silicone rubber is prepared using a two-component kit (Sylgard 184) purchased from Dow Corning (Midland, MI) (see [9] for details). The rubber block (green) is attached to a metal block (black) on the upper surface, as indicated in figure 1(b).

The rubber block has seven ribs with radius $R = 0.75$ mm and an individual length of 30 mm. The normal force is kept constant for all experiments at $F_N \approx 24.6$ N, resulting in a Hertz contact width $w \approx 0.4$ mm and Hertz average pressure at the interface between the ribs and the substrate of $\sigma_N \approx 0.3$ MPa. The substrate is covered with fluids of varying viscosities (from $\eta = 0.001$ Pa s (water) to 1.48 Pa s (glycerol)). With increasing squeezing time the fluids get removed from the nominal rib–substrate contact region [9, 10]. The decrease in the film thickness and the increase in the contact area with increasing time of stationary contact results in a breakloose friction force (at a given fixed drive velocity v) which increases with the time of stationary contact. In our experiments, after waiting some given time period, the substrate surface is moved perpendicular to the ribs with a constant velocity $v \approx 1.0$ mm s^{-1} (drive velocity). Figure 2 shows an example of the friction force as a function of time after a 10 min squeeze-out time. The decrease in the friction at the onset of slip is due to the increase in the fluid film thickness between the ribs and the substrate during sliding (mixed lubrication). That is, during sliding, the rubber ribs deform in such a way as to form tilted surfaces at the interface which facilitate the build up of a hydrostatic fluid pressure which keeps the surfaces separated [14].

The final experiment (c) was performed at BD Franklin Lakes. Here we have measured the breakloose friction for syringes as a function of the time of stationary contact. In these experiments the ribs of the rubber stopper are squeezed against the lubricated (with a silicone oil) barrel surface. The barrel is made from a polymer or from glass. Due to fluid squeeze-out the breakloose friction force increases continuously with the time of stationary contact. The elastic modulus of the bromobutyl rubber in the stopper is $E \approx 3$ MPa. In these experiments the width of the rib–barrel contact region is $w \approx 0.7$ mm and the average contact pressure $\sigma_N \approx 1$ MPa. This application involves the slowest fluid squeeze-out, and even after waiting 907 days (or $\approx 10^8$ s) the area of real contact is below the percolation threshold.

Table 1. Properties of the three squeeze-out systems. The surface root-mean-square (rms) slope ξ and rms roughness amplitude h_{rms}. The average contact pressure P and the relative contact area (dry surfaces) A/A_0. Fluid viscosity $\eta \approx 1$–10 Pa s and surface anisotropy Tripp number $\gamma = 1$.

System	ξ	h_{rms} (μm)	P (MPa)	A/A_0	Squeeze-out
Ball–flat	1.1	2.7	0.2	0.15	Fast
Rib–flat	0.28	1.6	0.3	0.93	Slow
Syringe	0.5–0.7	8.3	0.8	0.6–0.8	very slow

In table 1 we summarize some of the properties of the systems studied below. Fluid squeeze-out is fast when the surface roughness is large enough or the nominal pressure small enough so that the contact area in the absence of the fluid is below the percolation limit. Note that the area of contact is determined mainly by the short wavelength roughness, which also determines the root-mean-square (rms) slope ξ of the surface. Thus, it is the rms slope ξ and not the rms roughness amplitude h_{rms} which matters for the time dependence of the area of real contact. However, if the interfacial energies are such that dewetting occurs, then the increase in the area of real contact is fast also for very smooth surfaces with $\xi \approx 0$ (see [19–21]). In this latter case, at least if the nominal pressure is not too high, the dewetting will nucleate close to the center of the contact area and spread radially [19–21]. Thus, experiments have shown that for smooth PDMS balls (radius of the order of ~1–2 mm) in silicone oil with a viscosity ~1–5 Pa s, squeezed against a passivated glass surface with a nominal pressure ~0.1 MPa, fluid removal resulting in a dry (adhesive) contact prevails after ~100 s or less [21]. However, depending on the line tension and squeeze-rate (or loading force) a more complex squeeze-out pattern may form, resulting in (temporarily) trapped fluid islands and a slower squeeze-out [21, 41]. The slowest increase in the area of real contact may occur for an intermediate surface roughness, where ξ is not too large and not too small. For the systems studied here the very slow squeeze-out for the syringe may also be related to a very slow onset of dewetting (for polymer barrel) or perhaps no dewetting at all (for glass barrel).

3. PDMS ball on flat: low relative area of contact

We consider first a PDMS rubber hemisphere (radius $R = 1.5$ mm) in contact with a flat smooth glass surface. The

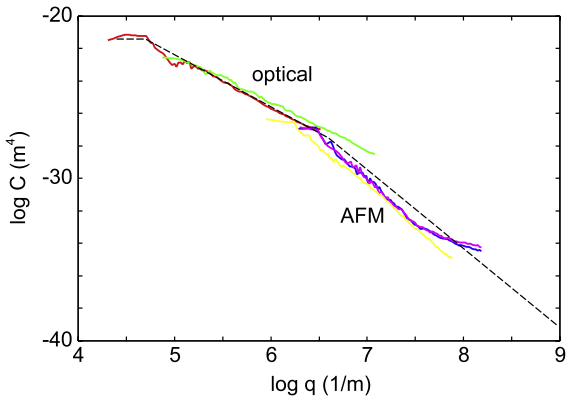

Figure 3. The surface roughness power spectrum of the PDMS hemisphere as obtained from optical and AFM measurements of the height profile. The dashed line is used in the contact mechanics calculations. Within the accuracy of the experiment the ball surface appears to have isotropic statistical properties. The dashed line corresponds to a surface with an rms roughness $h_{\rm rms} = 2.7\ \mu$m and an rms slope $\xi = 1.1$. The slope of the dashed line in the optically measured region corresponds to a fractal dimension $D_{\rm f} = 2.34$.

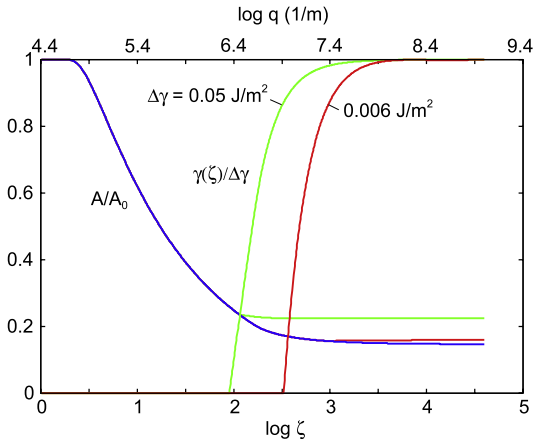

Figure 4. The (relative) area of real contact, A/A_0, as a function of the magnification. Also shown is the effective interfacial binding energy, $\gamma(\zeta)/\Delta\gamma$ (in units of the interfacial energy for flat surfaces $\Delta\gamma$) as a function of the wavevector $q = q_0\zeta$ of the smallest wavevector included in the calculation. That is, all roughness components with wavevectors between q and q_1 are included (where $q_1 = 10^9$ m^{-1} is the largest (cut-off) wavevector). The red and green lines are for $\Delta\gamma = 0.006$ J m^{-2} and 0.05 J m^{-2}, respectively, and with $E = 2.2$ MPa and $\sigma_{\rm N} = 0.2$ MPa. The blue line is the contact area without adhesion. The relative contact areas at the highest magnification are 0.22 and 0.16 for $\Delta\gamma = 0.05$ J m^{-2} and 0.006 J m^{-2}, respectively. In the absence of adhesion ($\Delta\gamma = 0$) (blue line) the relative contact area at the highest magnification is 0.15.

surface roughness of the rubber hemisphere was so large and the nominal contact pressure so small that the (dry) area of real contact is only ∼15% of the nominal contact area. For lubricated contacts, this results in percolation of large interfacial fluid flow channels and to fast fluid squeeze-out. This differs from the other two systems studied below, where the surface roughness is smaller and the nominal contact pressure higher, and where the dry contact area is nearly equal to the nominal contact area. In these cases the area of real contact during fluid squeeze-out will percolate, resulting in very slow fluid squeeze-out.

3.1. Surface roughness power spectra

The topography of the rubber hemispheres was measured using optical microscopy and atomic force microscopy (AFM). Figure 3 shows the surface roughness power spectrum of the PDMS hemispheres as calculated from the measured height profiles. The dashed line is a fit to the experimental data used in the contact mechanics calculations presented below. Within the accuracy of the experiment the ball surface appears to have isotropic statistical properties. The dashed line in figure 3 corresponds to a surface with an rms roughness $h_{\rm rms} = 2.7\ \mu$m and an rms slope $\xi = 1.1$.

3.2. Dry contact mechanics

In the theory developed in [15, 16] one of us has studied the dependence of the area of contact, $A(\zeta)$, and the interfacial binding energy per unit surface area, $\gamma(\zeta)$, on the magnification ζ. When we calculate the contact area $A(\zeta)$ at a magnification ζ it is assumed that no surface roughness with wavevectors $q > \zeta q_0$ exists, i.e., the surfaces appear smooth at length scales shorter than $\lambda = 2\pi/q = 2\pi/(q_0\zeta)$. As the magnification increases more roughness is observed and the area of (apparent) contact decreases. The nominal or apparent contact area $A_0 = A(1)$ is the contact area observed at the lowest magnification, where the surfaces appear smooth. The true (atomistic) contact area $A_1 = A(\zeta_1)$ is the contact area observed at the highest magnification ζ_1, where all the surface roughness components are taken into account. $\gamma(\zeta)$ is the interfacial binding energy (per unit area) in the contact area $A(\zeta)$, when the interface is studied at a magnification ζ. It follows that $\gamma(\zeta_1) = \Delta\gamma = \gamma_1 + \gamma_2 - \gamma_{12}$, while $\gamma(1) = \gamma_{\rm eff}$ is the effective macroscopic interfacial energy in the surface area $A_0 = A(1)$, which is the quantity entering in, e.g., the JKR theory. Thus, if $\gamma(1) = 0$ the (adiabatic) pull-off force will vanish, i.e., no adhesion will manifest itself directly at the macroscopic scale. In the present application for dry surfaces $\Delta\gamma \approx 0.05$ J m^{-2}, as expected for the PDMS–glass interface at thermal equilibrium. For the experiment in water we use the same $\Delta\gamma \approx 0.05$ J m^{-2}, while in silicone oil $\Delta\gamma \approx 0.006$ J m^{-2} (see [17]).

Note that even if $\gamma(1) = 0$, the interfacial adhesion does increase the contact area when the load (or squeezing pressure) is non-vanishing. This is illustrated in figure 4 for the rough PDMS hemisphere squeezed against a flat smooth glass substrate, at the average (or normal) pressure $\sigma_{\rm N} = 0.2$ MPa. The figure shows the variation of the relative area of contact, $A(\zeta)/A_0$, and the relative effective interfacial energy $\gamma(\zeta)/\Delta\gamma$, with the logarithm of the magnification $\zeta = q/q_0$, for dry surfaces and for surfaces lubricated with water and silicone oil after a long contact time (thermal equilibrium condition). Note that for dry surfaces and magnifications larger than $\zeta_{\rm c} \approx 100$ the contact area becomes approximately independent of the magnification, i.e., the surfaces are in

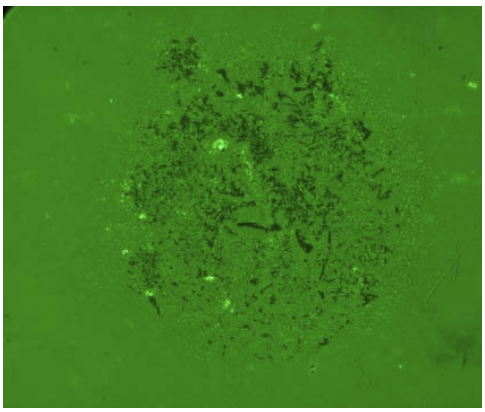

Figure 5. Contact region between a PDMS ball and a smooth glass countersample (black). The PDMS hemisphere radius $R = 1.5$ mm and the diameter of the Hertzian contact region is 0.55 mm. The rubber hemisphere was made by cross-linking against a rough aluminum mold. The aluminum negative had a hemispherical hole that was sandblasted for surface roughness. The average Hertz pressure is $\sigma_N \approx 0.2$ MPa. The relative contact area $A/A_0 \approx 0.15$ (where $A_0 = \pi r_0^2$ is the nominal contact area).

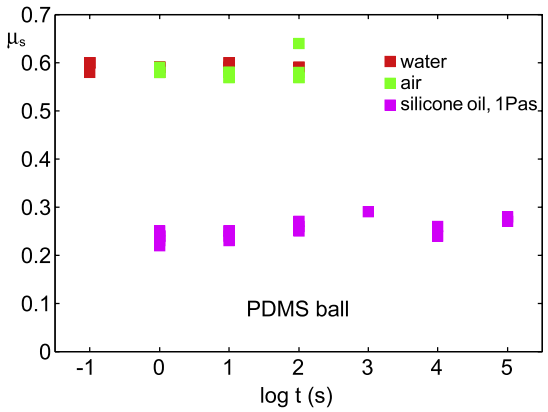

Figure 6. The dependence of the breakloose friction force on the time of stationary contact for dry surfaces, and for surfaces in water and in silicone oil (viscosity $\eta = 1.0$ Pa s). The drive velocity $v = 0.1$ mm s^{-1}.

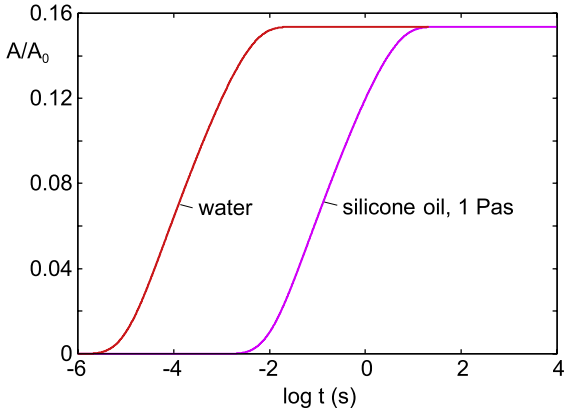

Figure 7. The area of contact A (in units of the nominal contact area A_0) as a function of the time of stationary contact for a PDMS ball on glass lubricated by water (viscosity $\eta = 0.001$ Pa s) (red line) or by silicone oil (viscosity $\eta = 1.0$ Pa s) (magenta line).

nearly complete contact within the asperity contact regions which can be observed at a magnification ζ_c. In the absence of adhesion (blue line) the contact area would instead continue to decrease as the magnification increases beyond ζ_c, as new shorter wavelength roughness now would be observed.

When the dry contact interface is observed using optical microscopy at the highest magnification (corresponding to ~ 1 μm resolution or a magnification of the order of $\zeta \approx 10^3$), see figure 5, the relative contact area within the nominal Hertz contact region can be calculated to be $A/A_0 \approx 0.15$. This is in excellent agreement with the theory prediction for $A(\zeta)/A_0$ at the corresponding magnification $\zeta \approx 10^3$ (see figure 4), where $A(\zeta)/A_0 \approx 0.15$–$0.22$ depending on the $\Delta\gamma$ used (note: the thermodynamic $\Delta\gamma \approx 0.05$ J m^{-2}, but for a closing crack (which prevails during contact formation) the effective $\Delta\gamma$ may be smaller depending on the contact time).

3.3. Breakloose friction for dry surfaces

The green squares in figure 6 show the dependence of the breakloose friction force on the time of stationary contact for dry surfaces. There is almost no dependence of the breakloose friction force on the time, which differs from measurements we performed on other types of rubber. We attribute this to the nearly elastic behavior of the PDMS rubber (no or negligible viscoelastic creep), in contrast to most other types of rubber. If we write the normal force as $F_N = \sigma_N A_0$ and the breakloose friction force as $F_s = \tau_s A$, where A is the area of real contact and τ_s the effective (or average) frictional shear stress acting in the area of real contact, then since the friction coefficient $\mu_s = F_s/F_N$ we get (see also section 3.5 below)

$$\tau_s = \mu\sigma_N(A_0/A). \tag{1}$$

Since $A/A_0 \approx 0.15$ (from theory and experiment) and $\mu \approx 0.6$ and $\sigma_N \approx 0.2$ MPa, we get $\tau_s \approx 0.82$ MPa for the drive velocity $v = 0.1$ mm s^{-1}.

3.4. Breakloose friction for lubricated surfaces

The red and magenta squares in figure 6 show the dependence of the breakloose friction force on the time of stationary contact for surfaces in water (viscosity $\eta = 0.001$ Pa s) and in silicone oil (viscosity $\eta = 1.0$ Pa s), respectively. Note again that there is almost no dependence of the breakloose friction coefficient on the time of stationary contact. This results from the fast fluid squeeze-out. Thus in figure 7 we show the calculated variation of the area of real contact on the time after the squeezing force was applied [9, 10, 18]. The initial separation between the surfaces was 100 μm, but the squeeze-out for large surface separation occurs very fast and the initial separation, as long as it is much larger than the rms roughness amplitude, has negligible influence on the result in figure 7. Note that both in water and in silicone oil the contact area is close to the final asymptotic contact area already at the shortest time measured in figure 6 (0.1 s in water and 1 s in silicone oil). The fast squeeze-out is related to the low contact area, which results in many large interfacial flow channels even after long contact times where the contact area reaches

its maximum. In the calculation in figure 7 we have neglected the adhesion (see below), so that the final (long contact time) relative contact area is $A/A_0 \approx 0.15$ (blue line in figure 4).

The contact regions in both water and silicone oil are likely to be dry. This is expected because experiments [17] have shown that the interfacial energy $\Delta\gamma = \gamma_{SL} + \gamma_{RL} - \gamma_{SR}$ (S = solid = glass, R = rubber, L = liquid) is positive for silicone rubber in contact with glass in both water and in silicone oil, and one expects dewetting transitions to occur in both cases. Due to the small size of the asperity contact regions (in the dry state, see figure 5) one expects very fast dewetting transitions once nucleated. For silicone rubber against glass in silicon oil $\Delta\gamma$ is rather small (about $\Delta\gamma \approx 0.006$ J m^{-2}) while in water $\Delta\gamma$ is similar to the dry state [17], namely $\Delta\gamma \approx 0.05$ J m^{-2}. The time it takes to dewet an asperity contact region is of the order of [19–22]

$$\Delta t \approx 8.5 \left(D^4 h \left(\frac{E}{\Delta\gamma} \right)^2 \right)^{1/3} \frac{\eta}{\Delta\gamma},$$

where h is the fluid film thickness at the point of nucleation of the dewetting transition and D the linear size of the asperity contact regions. This equation was derived for smooth surfaces and may only be approximately valid in the present case where the surfaces are rough also on length scales smaller than the size D of the contact regions. In the present case the contact regions are very small, of the order of $D \approx 1$ μm (see figure 7), and assuming $h \approx 10$ nm we get $\Delta t \approx 10^{-7}$ s in water and $\approx 10^{-3}$ s in silicone oil. Thus we expect both squeeze-out and dewetting to occur so fast as to result in dry contact regions on the time scales of the measurements in figure 6.

From the experimental data in figure 6 and the calculated (thermal equilibrium) contact area $A/A_0 = 0.16$ and 0.22 (in silicone oil and water, see figure 4), using (1) we obtain the frictional shear stress $\tau_s = 0.55$ MPa in water and $\tau_s = 0.31$ MPa in silicone oil.

Since the interfacial binding energy (per unit area) $\Delta\gamma \approx 0.05$ J m^{-2} in water is nearly the same as in the dry state, one expects A/A_0, after long enough contact time, to be nearly identical in water as to in the dry state, which is consistent with the friction coefficients observed for both systems (see figure 6). However, in silicone oil the interfacial binding energy is nearly zero, the area of real contact is smaller than for dry contact, and the friction coefficient consequently smaller than for the dry state or in water. However, even taking this into account we have found above that the calculated frictional shear stress in the (dry) contact area is smaller in silicone oil ($\tau_s = 0.31$ MPa) than in water ($\tau_s = 0.55$ MPa). We will now address this problem.

3.5. Discussion

For the systems studied above (PDMS ball in contact with glass lubricated by water or silicone oil) we expect dewetting to occur, resulting in dry contact areas. Nevertheless, the effective frictional shear stress we deduce is smaller in silicone oil ($\tau_s \approx 0.31$ MPa) as compared to in water ($\tau_s \approx 0.55$ MPa). In addition all these values are considerably larger than obtained in section 4.3 for a different situation where complete contact occurs between the rubber and the substrate within the nominal contact region (a Hertz line-contact) ($\tau_s \approx 0.2$ MPa). In this section we will propose an explanation of this important observation.

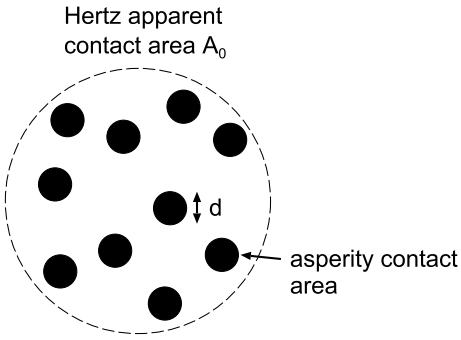

Figure 8. The N asperity contact regions within the Hertz apparent contact area A_0 have the total contact area $A = N\pi d^2/4$.

There are two contributions τ_A and τ_B to the effective frictional shear stress, $\tau_s = \tau_A + \tau_B$. The first τ_A is derived from breaking and forming bonds within the rubber–substrate contact regions, and will be proportional to the contact area A, at least if the bonds are broken uniformly at the onset of slip (see section 4.5). The second contribution τ_B is derived from the edges or boundaries of the contact region, which can be considered as crack-like defects. In particular, the exit side of the contact regions can be considered as opening cracks and the energy dissipation here may contribute in an important way to the effective frictional shear stress, in particular when the contact regions are of a small linear size d. Let us for simplicity assume that the contact area consists of many small circular regions of diameter d, see figure 8. If there are N such microscopic contact regions the contact area $A = N\pi d^2/4$. When the contact has slid a distance L the opening crack will have passed over the total area NLd, which will result in an energy dissipation $NLdG(v)$, where $G(v)$ is the crack propagation energy per unit surface area. Thus if the contribution to the friction force from the crack opening process is denoted by F_B we get $F_B L = NLdG(v)$ or $F_B = G(v)4A/(\pi d)$, and the contribution to the effective frictional shear stress from the opening cracks will be $\tau_B = 4G(v)/(\pi d)$. One can estimate that for PDMS at the sliding velocity $v \approx 0.1$ mm s^{-1} and without lubrication fluid we have $G(v) \approx 0.4$ J m^{-2}, and with $d \approx 1$ μm as the typical linear size of the contact regions in the present case (see figure 5) we get $\tau_B \approx 0.5$ MPa, which is of similar magnitude to the observed frictional stress. Note, however, that when the surface roughness is small enough, the contact regions will be compact (i.e., $N = 1$). For this case, using parameters relevant for our applications (linear size of contact region $d = 200$ μm and sliding velocity $v = 1$ mm s^{-1}), the contribution to the shear stress from the opening crack would be very small, $\tau_B \approx 0.001$ MPa, which can be neglected compared to the contribution from breaking and forming bonds within the contact region, which gives $\tau_A \approx 0.2$ MPa (see section 4.3).

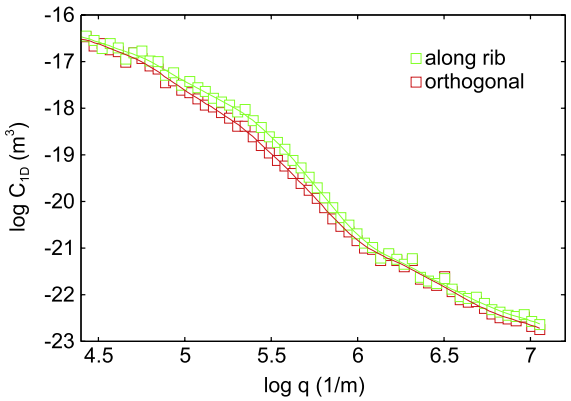

Figure 9. The 1D surface roughness power spectrum parallel and orthogonal to the ribs. The solid lines are fits to the experimental data. Within the accuracy of the experiment the rib surface appears to have isotropic statistical properties. The rib rms roughness $h_{\rm rms} = 1.58$ μm and 1D rms slope $\xi = 0.20$.

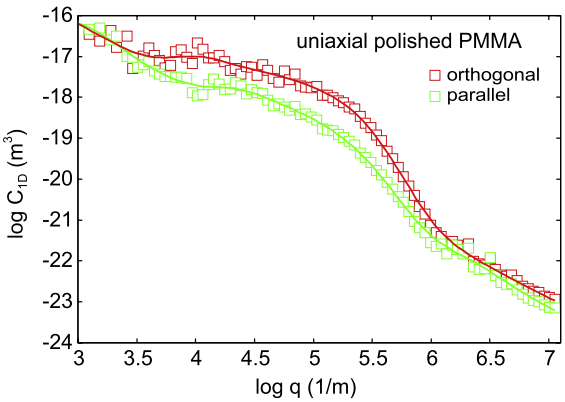

Figure 10. The 1D surface roughness power spectrum of the uniaxially ground PMMA surface along and orthogonal to the grinding direction (squares). The solid lines are fits to the experimental data. The surface rms roughness $h_{\rm rms} \approx 1$ μm and the 1D rms slope $\xi = 0.20$ orthogonal to the wear tracks and 0.14 parallel to the wear tracks.

For the PDMS–glass system in water the effective interfacial binding energy $\Delta\gamma$ is nearly the same as in the dry state, so we expect similar contributions to τ_B for these two cases. For the PDMS–glass system in silicone oil $\Delta\gamma$ is smaller than in water (or in the dry state), and we expect a smaller τ_B for this case, in qualitative agreement with observations.

4. PDMS cylinder ribs on flat: high relative contact area

In the study above the surface roughness was so large (and the squeezing force so small) that the area of real contact only constitutes ∼15% of the nominal Hertzian contact area. In this section we will consider another system where the opposite is true and the area of contact (for dry surfaces) is nearly equal to the nominal contact area. When the relative contact area A/A_0 becomes higher than ≈0.42, the contact area will percolate, which will result in confined fluid regions, and a drastic slow down of the squeeze-out (see [38]). Thus, in the absence of dewetting transitions the contact area would saturate at 42% of the nominal contact area, but if dewetting occurs the contact area can approach 100% contact. However, we find that even when dewetting occurs the squeeze-out of the fluid is drastically slowed down compared to the case where the final (asymptotic long time) contact area is a small fraction of the nominal contact area.

4.1. Surface roughness power spectra

Using a stylus instrument we have measured the surface topography of the mold used for producing the ribs of the rubber block, and of all the substrate surfaces. Line scans were performed parallel and orthogonal to the ribs. From the height topography we calculated the 1D surface roughness power spectrum, see figure 9. The solid lines are fits to the experimental data. Within the accuracy of the experiment the rib surface appears to have isotropic statistical properties. Including the surface roughness wavevector components shown in figure 9 the surface rms roughness $h_{\rm rms} = 1.58$ μm and 1D rms slope $\xi = 0.20$.

In the experiments both flat and rough substrate surfaces are used. The rough substrate surfaces are produced by uniaxial lapping with sandpaper of PMMA (we will refer to the surfaces as ground), giving an anisotropic roughness. In figure 10 we show the 1D surface roughness power spectrum of the uniaxially ground PMMA surface along and orthogonal to the grinding direction (squares). The solid lines are fits to the experimental data. The surface rms roughness $h_{\rm rms} \approx 1$ μm and the 1D rms slope $\xi = 0.20$ orthogonal to the wear tracks and 0.14 parallel to the wear tracks.

In the calculations presented below we have used the 2D-power spectrum calculated from the 1D-power spectrum as described in [23], and also extended the power spectrum linearly (on the log–log scale) to the large wavevector cut-off $q_1 = 10^9$ m^{-1}. The extrapolated part has the fractal dimension $D_{\rm f} = 2$ and joins smoothly to the measured power spectrum for smaller wavevectors.

4.2. Dry contact mechanics

We now present numerical results for the relative area of contact, A/A_0, obtained from adhesion calculations for the PDMS ribs in contact with the ground PMMA surface. We have used the interfacial binding energy (per unit surface area) for flat surfaces $\Delta\gamma = 0.05$ J m^{-2}, the PDMS Young's modulus $E = 2.2$ MPa and $\sigma_{\rm N} = 0.3$ MPa. In figure 11 the red lines show the (relative) area of contact as a function of the magnification. The dashed line is without adhesion and the solid line is with adhesion included. The true (atomic) contact area is the contact area observed at the highest magnification ζ_1. Note that when adhesion is included the contact is nearly complete $A(\zeta_1)/A_0 \approx 0.93$, while in the absence of adhesion $A(\zeta_1)/A_0 \approx 0.57$. For the PDMS ribs in contact with the smooth surfaces the contact area is even larger, and, in particular, complete contact occurs when adhesion is included.

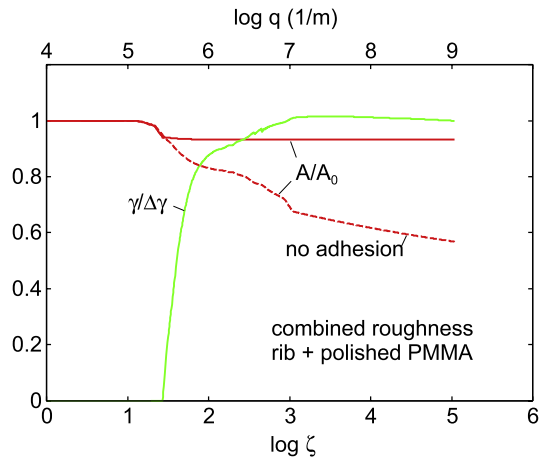

Figure 11. Red line: the (relative) area of contact as a function of the magnification. The dashed line is without adhesion and the solid line with adhesion included. Green line: the effective interfacial energy $\gamma(\zeta)$ (in units of the interfacial energy for flat surfaces $\Delta\gamma$) as a function of the wavevector $q = q_0\zeta$ of the smallest wavevector included in the calculation, i.e., all roughness components with wavevectors between q and q_1 are included (where $q_1 = 10^9$ m^{-1} is the largest (cut-off) wavevector). For the PDMS ribs in contact with the ground PMMA surface. We have used $\Delta\gamma = 0.05$ J m^{-2}, $E = 2.2$ MPa and $\sigma_N = 0.3$ MPa.

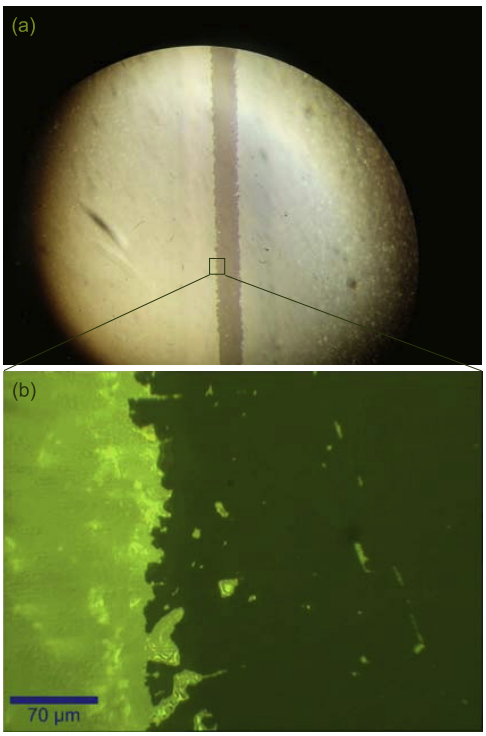

Figure 12. Optical pictures of a PDMS rib squeezed in contact with a flat glass substrate. (a) Low magnification picture: the dark vertical strip is the rib–glass contact region of width $w \approx 0.4$ mm. (b) Higher magnification picture of the rib contact close to one edge of the contact strip. The dark green area is contact and the light green area is non-contact. Note that the boundary line between contact and non-contact is rough due to the surface roughness of the rib.

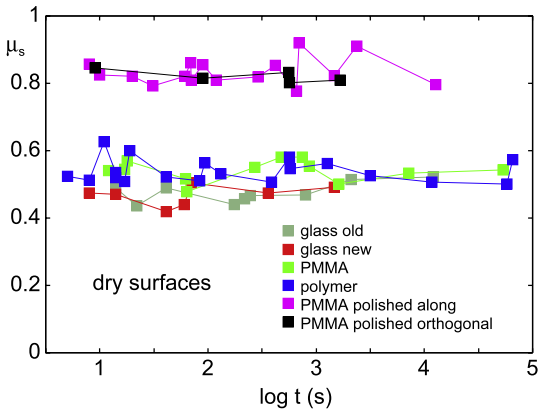

Figure 13. The dependence of the breakloose friction force on the time of stationary contact for dry surfaces.

The green line in figure 11 shows the effective interfacial energy $\gamma(\zeta)$ (in units of $\Delta\gamma$) as a function of the wavevector $q = q_0\zeta$ of the smallest wavevector included in the calculation (so that wavevectors between q and q_1 are included, where $q_1 = 10^9$ m^{-1} is the largest (cut-off) wavevector). Note that the macroscopic interfacial binding energy $\gamma_{\text{eff}} = \gamma(1) = 0$, i.e., the (slow, adiabatic) pull-off force vanishes.

Figure 12 shows optical pictures of a PDMS rib squeezed in contact with a flat glass substrate. Figure 12(a) shows a low magnification picture, where the rib–glass contact area appears as the dark vertical strip. Figure 12(b) shows a higher magnification picture of the rib contact close to one edge of the contact strip. The dark green area is contact and the light green area non-contact. Note that the boundary line between contact and non-contact is rough due to the surface roughness on the rib. However, in accordance with the theory prediction, within the (nominal) contact region the contact is nearly complete—e.g., even close to the edges of the contact, where the normal stress is negative due to the adhesive interaction. For the PDMS rib in contact with the rough PMMA surface, the optical image (not shown) is less clear (blurred), but consistent with ∼90% contact as predicted by the theory.

4.3. Breakloose friction for dry surfaces

Let us first study the PDMS ribs sliding on dry smooth glass, PMMA and inert polymer (cyclo-olefin) surfaces, as well as on ground (roughened) PMMA. Figure 13 shows the measured breakloose friction coefficient for all surfaces. Note that, remarkably, the friction values on all the smooth surfaces have similar magnitudes and are independent of the time of stationary contact—i.e., negligible ageing (e.g., viscoelastic relaxation) occurs. On the ground (rough) PMMA surface the friction coefficient is nearly twice as high as on the smooth PMMA. (After a very long contact time (3 days) the breakloose friction on the rough PMMA was reduced due to transfer of free PDMS chains to the substrate (see appendix B).) As discussed in appendix C, the viscoelastic contribution to the friction coefficient from the pulsating deformations of the rubber surface from the substrate asperities is rather small (of the order of 0.05) and cannot explain the higher friction on the rough surface. From the measured friction coefficients one can deduce the

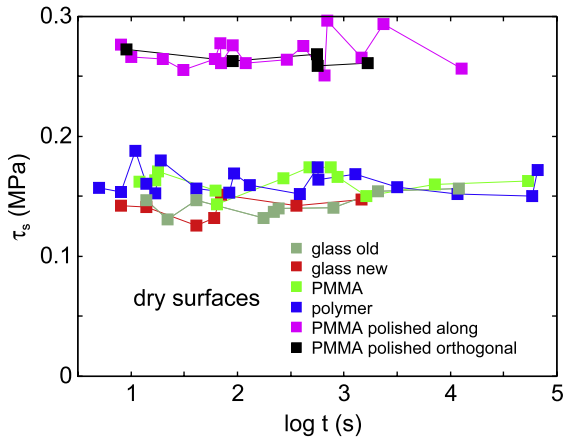

Figure 14. The dependence of the interfacial frictional shear stress τ_s on the time of stationary contact for dry surfaces.

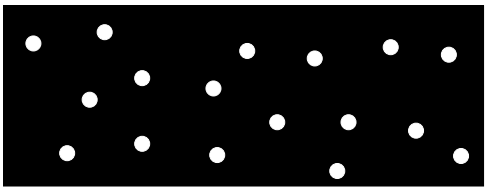

Figure 15. Picture of the contact (black region) between a PDMS rib and the rough PMMA substrate. The contact is incomplete (about ∼10% non-contact) and during sliding the opening crack at the contact–non-contact boundary line will result in energy dissipation and contribute to the observed effective frictional shear stress.

breakloose frictional shear stress τ_s in the area of real contact A, using (see (1) and below): $\tau_s = \mu\sigma_N(A_0/A)$, where A_0 is the nominal contact area, and where A has been calculated using the Persson contact mechanics theory.

In figure 14 we show the breakloose frictional shear stresses for the systems studied in figure 13. Here we have used $A/A_0 = 0.93$ for the ground PMMA surface and $A/A_0 = 1$ for the other surfaces. On the ground (rough) PMMA surface the frictional shear stress (≈0.27 MPa) is nearly twice as high as on the smooth PMMA (≈0.15 MPa). This result is similar to observations in [24], where the kinetic frictional shear stress measured on flat glass and slightly roughened glass was $\tau_k \approx 0.1$ MPa and $\tau_k \approx 0.2$ MPa, respectively.

The larger frictional shear stress on the rough PMMA may be due to two different mechanisms. Figure 15 shows a schematic picture of the contact (black region) between a PDMS rib and the rough PMMA substrate. The contact is incomplete (about ∼10% non-contact, white circular regions) and during sliding the opening crack at the contact–non-contact boundary line will result in energy dissipation and contribute to the observed effective frictional shear stress.

Figure 16 illustrates another mechanism which we believe may contribute to why the friction is larger on the roughened PMMA surfaces. Figure 16(a) shows PDMS sliding on an atomically smooth surface, and (b) on a surface with very short-range (atomic) roughness. On the smooth surface the energetic barrier for lateral slip is small, while it is larger on the atomically rough surface, leading to larger pinning barriers for the polymer chains and thus to a higher frictional shear stress.

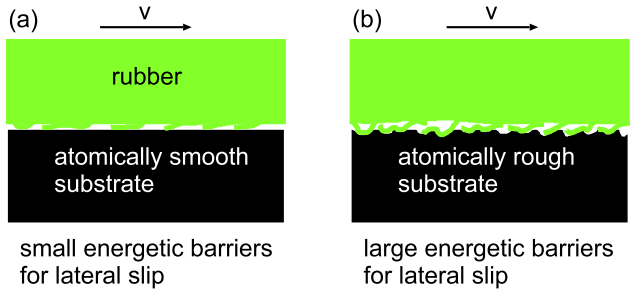

Figure 16. PDMS sliding on an atomically smooth surface (a), and on a surface with very short-range roughness (b). On the atomically rough surface the energetic barriers for lateral slip are higher than on the smooth surface, leading to larger pinning barriers for the polymer chains and thus to a higher frictional shear stress.

For the PDMS ribs on smooth dry glass we observe after breakloose a constant kinetic friction force (no stick–slip) $F_k \approx 0.6F_s$ at the sliding velocity $v \approx 1$ mm s^{-1}. This is consistent with the standard picture [25–29] of the origin of rubber friction on smooth surfaces as resulting from molecular bridges from the rubber binding to the hard substrate by weak bonds, e.g., van der Waals bonds or hydrogen bonds. After a bond is broken during sliding it takes some relaxation time t_{on} to reform the bond with the substrate, so that when the sliding velocity increases the number of bonds will decrease. In fact for PDMS on glass in [17, 30] it has been argued that $\tau_k \approx \tau_s/(1 + v/v^*)$, where $v^* = \delta/t_{on}$ and δ is the maximum extension of a bond at rupture. With $\delta \approx 1$ nm and $t_{on} \approx 10^{-6}$ s of the order of the Rouse time (as expected for a weak van der Waals type of interaction) one can estimate [17, 30] $v^* \approx 1$ mm s^{-1}, which would give a kinetic frictional shear stress $\tau_k \approx 0.5\tau_s$, which is consistent with our observations. In addition, since $t_{on} \ll 1$ s no time dependence (ageing) of the breakloose friction is expected in our systems on the time scales of our measurements, in good agreement with observations (see figures 13 and 14).

4.4. Breakloose friction for lubricated surfaces

We now consider the rubber ribs squeezed against a smooth substrate in a fluid with viscosity $\eta = 1$ Pa s. The nominal (average) Hertz contact pressure $\sigma_N = 0.3$ MPa, the rubber elastic modulus $E = 2.2$ MPa and Poisson ratio $\nu = 0.5$. The ribs have the surface roughness power spectrum from figure 9 (but extrapolated to $q_1 = 10^9$ m^{-1}). Figure 17 shows the calculated dependence of the relative area of contact A/A_0 on the time of stationary contact. The red and green solid lines are calculated results using a theory which accounts for the surface roughness via a fluid pressure flow factor, which was calculated using the Persson contact mechanics theory in combination with the Bruggeman effective medium theory [36, 45] (see also section 5). The green line is the full elastohydrodynamic theory result, which also accounts for the

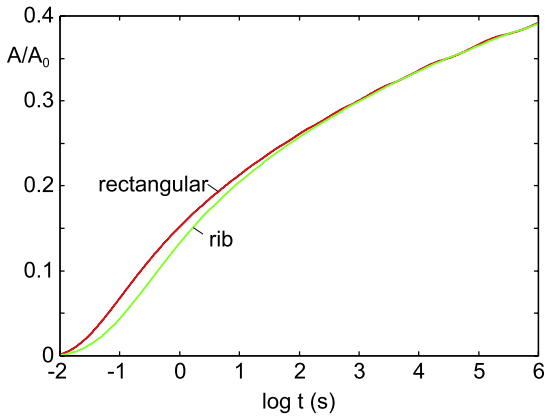

Figure 17. The calculated dependence of the relative area of contact A/A_0 on the time of stationary contact. The red and green solid lines are calculated results using theories which account for the surface roughness. The green line is the full elastohydrodynamic theory result, which also accounts for the bending of the bottom surface of the rib inwards as a result of the fluid pressure, while the red curve is for a flat (infinite) rectangular surface with the same width w as for the Hertz dry contact. The fluid viscosity $\eta = 1$ Pa s and the nominal contact pressure $\sigma_N = 0.3$ MPa. The elastic modulus $E = 2.2$ MPa and Poisson ratio $\nu = 0.5$.

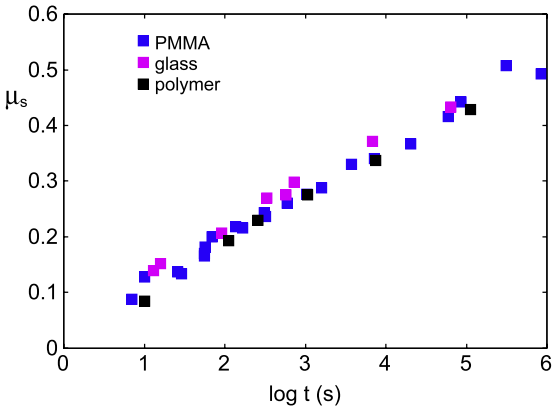

Figure 18. The dependence of the breakloose friction force on the time of stationary contact. The filled square symbols are the measured breakloose friction for the silicone rubber rib against a smooth PMMA, glass and (inert) polymer surface. In all cases the surfaces are lubricated with a silicone oil with viscosity $\eta = 1$ Pa s.

bending of the bottom surface of the rib inwards as a result of the fluid pressure [18], while the red curve is for a flat (infinite) rectangular surface with the same width w as for the Hertz dry contact [9, 10]. The theory used in deriving the results in figure 17 assumes that no dewetting transition occurs (see section 4.5).

Figure 18 shows the measured breakloose friction as a function of the logarithm (with 10 as basis) of time of stationary contact. The increase in the breakloose friction force with increasing time of stationary contact is due to the decrease in the film thickness and the increase in the contact area with increasing time of stationary contact. The blue, magenta and black squares show the results for the silicone rubber ribs on flat PMMA, glass and inert polymer

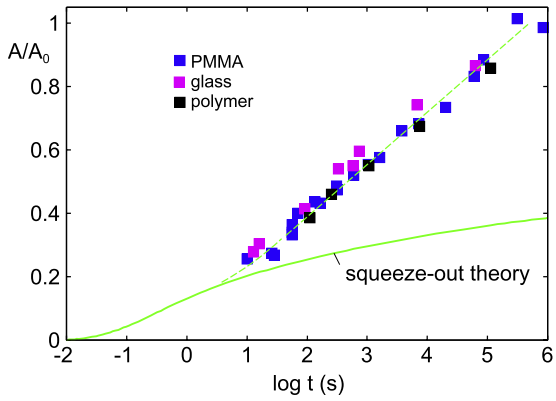

Figure 19. The area of contact A (in units of the nominal contact area A_0) as a function of the time of stationary contact. We have assumed that the asperity contact regions are dry with the breakloose frictional shear stress $\tau_s = 0.15$ MPa, as observed for dry surfaces (see figure 14). The filled square symbols are for the silicone rubber rib against a smooth PMMA, glass and (inert) polymer surface. The solid line is the result of the squeeze-out theory (no dewetting) (from figure 17). In all cases the surfaces are lubricated with a silicone oil with viscosity $\eta = 1$ Pa s.

(cyclo-olefin) surfaces, respectively, all lubricated by silicone oil with viscosity $\eta = 1$ Pa s.

To analyze the data we assume that the friction force is derived entirely from the area of real contact. If the frictional shear stress τ_s acting in the area of real contact was independent of the time of contact (no ageing) then $F_s = \tau_s A(t)$ and from (1):

$$A(t)/A_0 = \mu(t)(\sigma_N/\tau_s). \tag{2}$$

Using this formula and assuming dry asperity contact regions with the same breakloose shear stress τ_s as for dry surfaces, from figure 18 we get the relative contact area A/A_0 shown in figure 19. The green line in figure 19 is the theory prediction including only the squeeze-out dynamics (from figure 17). There are two possible reasons why $A(t)/A_0$ appears to increase faster with time than predicted by the theory: either the contact area does not saturate with increasing time as predicted by theory (see figure 17) and/or some molecular rearrangements must occur in the area of contact (ageing), resulting in a frictional shear stress which increases with the time of stationary contact[6]. However, since the friction coefficient (and the shear stress) for the dry surfaces does not depend on the time of stationary contact we believe that the origin of the increase in $A(t)$ beyond what is determined by the squeeze-out theory is due to dewetting driven by the lowering of the system free energy.

Figure 20 shows more results for smooth surfaces. Here the red and green symbols are the results using glass as a substrate with water–glycerol mixtures as lubricant with the viscosities 1.48 Pa s (pure glycerol) (red symbols) and 0.005 Pa s (green symbols). The upper symbols are for a dry substrate (glass, from figure 13). It is very surprising that for the water–glycerol $\eta = 0.005$ Pa s fluid (green symbols), for

[6] When ageing occurs $\tau_s(t)$ depends on time and one cannot strictly use equation (2) but rather something like $\mu = (\sigma_N A_0)^{-1} \int_0^t dt' A'(t') \tau_s(t - t')$.

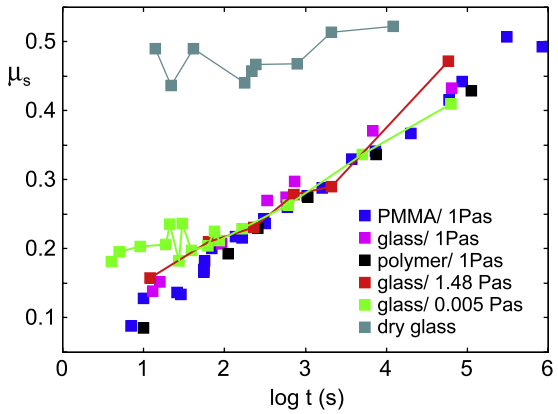

Figure 20. The dependence of the breakloose friction force on the time of stationary contact. The blue, magenta and black filled square symbols are the measured breakloose friction for the silicone rubber ribs against a smooth PMMA, glass and (inert) polymer surface, lubricated with silicone oil with viscosity $\eta = 1$ Pa s (from figure 18). The red and green symbols are the results using glass as substrate with water–glycerol mixtures as lubricant with viscosities 1.48 Pa s (pure glycerol) (red symbols) and 0.005 Pa s (green symbols). The upper symbols are for a dry glass substrate. It is very surprising that for the water–glycerol $\eta = 0.005$ Pa s fluid (green symbols), for $t > 100$ s the breakloose friction is the same as for the higher viscosity (1 and 1.48 Pa s) fluids.

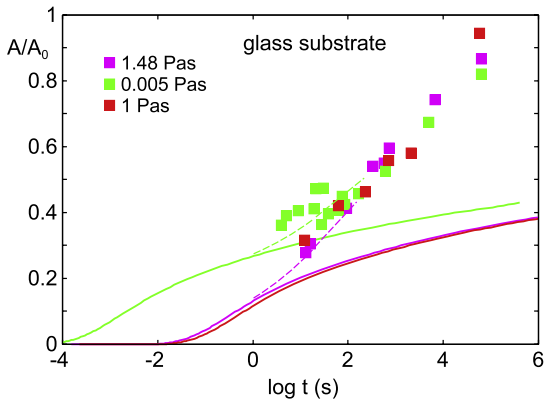

Figure 21. The area of contact A (in units of the nominal contact area A_0) as a function of the time of stationary contact for PDMS on glass. We have assumed that the asperity contact regions are dry, with the breakloose frictional shear stress $\tau_s = 0.15$ MPa, as observed for dry surfaces (see figure 14). The magenta square symbols are with a silicone oil lubricant with viscosity $\eta = 1$ Pa s (from figure 18), the green symbols with water–glycerol mixtures with viscosity $\eta = 0.005$ Pa s, and the red symbols for pure glycerol as lubricant with $\eta = 1.48$ Pa s. The solid lines are the result of the squeeze-out theory (no dewetting) (from figure 17 with the t-axis rescaled with the relevant viscosity).

$t > 100$ s the breakloose friction is nearly the same as for the higher viscosity (1 and 1.48 Pa s) fluids.

Figure 21 shows the dependence of the relative contact area $A(t)/A_0$ on the time of stationary contact for the silicone rubber ribs against a smooth glass substrate. The contact area A has been obtained from (2) using figure 20 and assuming $\tau_s \approx 0.15$ MPa to be the same as for dry surfaces. The magenta colored square symbols are for glass lubricated with a silicone oil with viscosity $\eta = 1$ Pa s (from figure 18), the green symbols for water–glycerol mixtures with $\eta = 0.005$ Pa s and the red symbols for pure glycerol with $\eta = 1.48$ Pa s. For all lubrication fluids one expects dewetting transitions [19, 20] to occur in the contact regions. That is, the lubricant is expelled from the contact regions, resulting in dry contact, as in the absence of a lubrication fluid. Wu-Bavouzet *et al* [17, 30] have shown that dewetting is expected for silicone oil and water–glycerol mixtures as lubricant between PDMS and glass (and passivated glass) substrates. They also observed for a PDMS ball sliding on a glass substrate a breakloose interfacial shear stress $\tau_s \approx 0.15$ MPa after a waiting time (determined by the period of the stick–slip motion) $t \approx 1$ s, which is similar to what we observe (see figure 21). Very similar dry contact shear stresses to those we observe have also been observed in [24, 31, 32] for smooth surfaces.

Figure 22 shows additional results for an uniaxially ground (roughened) PMMA surface lubricated by 1 Pa s silicone oil, and sliding along and orthogonal to the grinding direction. The friction is highest for sliding along the grinding direction, as indeed expected because of the faster fluid squeeze-out which occurs when the wear tracks are along the fluid flow direction. In this case there will also be a contribution to the friction from the viscoelastic deformations of the rubber surface by the substrate asperities. However,

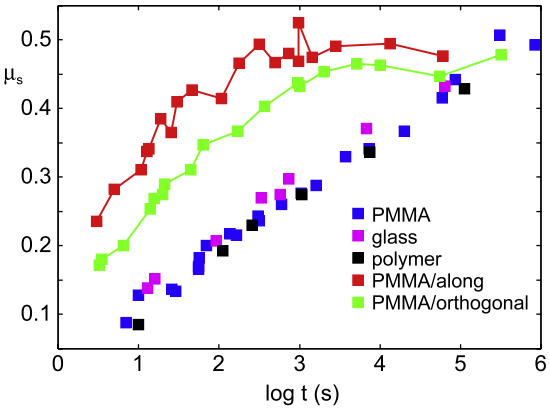

Figure 22. The dependence of the breakloose friction force on the time of stationary contact. The blue, magenta and black filled square symbols are the measured breakloose friction for the silicone rubber ribs against a smooth PMMA, glass and (inert) polymer surface (from figure 18). The red and green data points are for a uniaxially ground (roughened) PMMA surface sliding along and orthogonal to the grinding direction, respectively. In all cases the surfaces are lubricated with silicone oil with a viscosity $\eta = 1$ Pa s. The friction is highest for sliding along the grinding direction, as is expected because of the faster fluid squeeze-out in this case.

the study in appendix C indicates that this contribution to the friction coefficient is quite small, of the order of 0.05 on the dry surface.

Figure 23 shows the dependence of the relative contact area $A(t)/A_0$ on the time of stationary contact for PDMS on ground (roughened) PMMA. The results have been obtained from the measured breakloose friction coefficient (red and green data points in figure 22) using (2). Also shown (blue curve) is the relative contact area $A(t)/A_0$ (as in figure 17) calculated for a surface with an isotropic roughness power

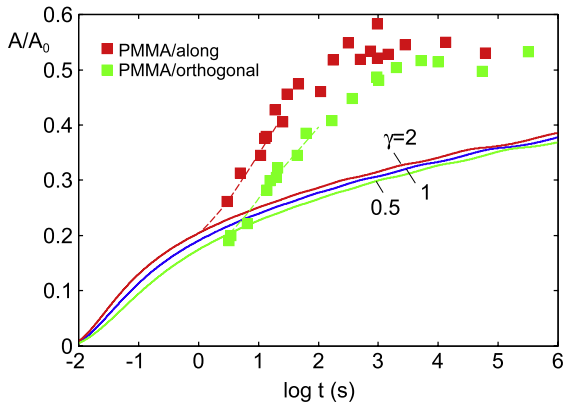

Figure 23. The area of contact A (in units of the nominal contact area A_0) as a function of the time of stationary contact for PDMS on ground (roughened) PMMA. We have assumed that the asperity contact regions are dry with the breakloose frictional shear stress $\tau_s = 0.27$ MPa, as observed for dry surfaces (see figure 14). The results have been obtained from the measured breakloose friction coefficient (red and green data points in figure 22) using (2). The solid lines are the contact area calculated (approximately) using the rectangular block approximation (as in figure 17), and with the power spectrum obtained by combining the (angular averaged) power spectrum of the uniaxially ground PMMA surface with that of the rubber ribs. Calculations were performed with the Tripp (asymmetry) numbers $\gamma = 1$ (corresponding to surface roughness with isotropic statistical properties), $\gamma = 0.5$ (corresponding to fluid flow orthogonal to the PMMA groves) and $\gamma = 2$ (corresponding to fluid flow parallel to the PMMA groves).

spectrum given by the angular averaged power spectrum of the uniaxially ground PMMA surface. Also shown are the results for two surfaces with an anisotropic roughness with Tripp numbers 2 and 0.5, but with the same angular averaged power spectrum as for the blue curve (with Tripp number 1). In the calculation we have used $\tau_s = 0.27$ MPa. As pointed out before, this shear stress is in accordance with measurements by Chateauminois *et al* [24], who observed about twice as high kinetic friction for PDMS on a rough glass surface as compared to a smooth glass surface, namely $\tau_k \approx 0.2$ MPa (rough) and $\tau_k \approx 0.1$ MPa (smooth). Note that the asymptotic (large time) contact area in figure 23 is smaller than that found in the calculation reported in figure 11 (solid red line) for dry surfaces, $A/A_0 \approx 0.93$, but very similar to what is predicted in the absence of adhesion (dashed line) $A/A_0 = 0.57$. This result is expected due to the weak, nearly vanishing, adhesion in the silicone oil.

4.5. Discussion

Equation (1) assumes implicitly that the interfacial bond-breaking occurs uniformly in the nominal contact area at the onset of slip. However, during the tangential loading, before breakloose, an interfacial (crack-like) slip region may propagate from the edges of contact towards the center of contact [24, 31–35]. If the slip distance $s(x, y, t)$ is smaller than the characteristic distance D necessary for the frictional stress to drop from its static value to the kinetic value then the slip will have a negligible influence on the breakloose friction force [7]. However, in the present case D may be of the order of δ, the maximum extension of a bond at rupture, which is only of the order of $\sim$1 nm. Nevertheless, a breakloose friction force larger than the kinetic friction force will still prevail if the slip velocity $v = \mathrm{d}s/\mathrm{d}t$ during the tangential loading before breakloose is much smaller than the drive velocity. Thus during loading when the slip velocity $\mathrm{d}s/\mathrm{d}t \ll v^*$ then the equation $\tau_k \approx 0.5\tau_s$ derived above would still hold. Experiments by Audry *et al* [32] indicate that for the contact between a glass ball and a PDMS rubber substrate, the interfacial slip, which occurs before the onset of breakloose, may only exist in a narrow region at the rim of the contact region. If this is the case also in our experiments then the main reason for the observation $F_k \approx 0.6F_s$ would still be strengthening of the bonds during the time of stationary contact, as discussed in section 3.2.

Let us now discuss the origin of the slow increase in $A(t)/A_0$ with the time of stationary contact for lubricated contact (see figures 21 and 23). In general, one expects a slow increase in τ_s with the time of stationary contact since a very long time may be necessary for the development of the maximum interfacial bond formation, i.e., no single relaxation time will characterize the bond formation but there may be other relaxation processes involving larger barriers and longer relaxation times than the t_{on} used above. However, for dry contact the time dependence of τ_s is negligible, see figure 14. Since, for lubricated contact, the area of real contact is assumed to be dry (dewetting), it is unlikely that the origin of the strengthening of the contact is due to an ageing process in the area of real contact. We therefore assume that there is an additional slow increase in the contact area beyond what is described by our squeeze-out theory. This may involve:

(a) the interdiffusion (flow) of lubricant molecules in the PDMS rubber, from the high pressurized fluid in the sealed-off regions to the region outside the nominal contact area, see figure 24. This process will reduce the fluid pressure in the confined regions, and hence also reduce the fraction of the load carried by the fluid, which will increase the contact area. Similar processes are know to occur in the lubrication of joints[7] [37]. However, while interdiffusion certainly will occur with silicone oil as lubricant, it should be much slower for the water–glycerol mixture. Since for pure glycerol the time dependence of $A(t)$ is similar to that of silicone oil (see figure 21) we believe that interdiffusion cannot explain the observed time dependence of $A(t)$ in the present case.

(b) Dewetting transitions in the asperity contact regions. Dewetting is known to occur for the fluid–solid systems

[7] The inner membrane of synovial joints is called the synovial membrane, secreting synovial fluid into the joint cavity. The fluid contains hyaluronic acid secreted by fibroblast-like cells in the synovial membrane and interstitial fluid filtered from the blood plasma. This fluid forms a thin layer (roughly $\sim$50 μm) at the surface of cartilage and also seeps into microcavities and irregularities in the articular cartilage surface, filling all the empty space. The fluid in articular cartilage effectively serves as a synovial fluid reserve. During movement, the synovial fluid held in the cartilage is squeezed out mechanically to maintain a layer of fluid on the cartilage surface (so-called weeping lubrication).

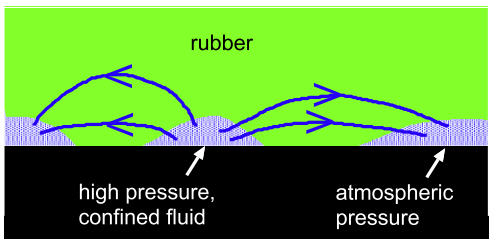

Figure 24. Fluid flow from high pressurized (confined) fluid regions to the (atmospheric pressure) fluid regions connected by percolating fluid flow channels to the outside region of the nominal contact area.

studied above, at least for smooth surfaces [17]. Dewetting involves the (thermally activated) nucleation of dry contact regions, which on macroscopic time scales may occur already for surface separations of the order of ∼10 nm. Dewetting involves the squeezed liquid accumulating in a rim at the edge of the dry contact area, which moves towards the edges of the nominal contact region, see figures 25(a) and (b). Hence, dewetting does not involve a global flow of fluid at the interface as described by the squeeze-out dynamics theory used above (figure 17). Thus, we visualize the squeeze-out as occurring via two very different processes: a global flow described by the theory used to calculate the results in figure 17, plus local dewetting transitions which nucleate close to the top of asperity contact regions when the film thickness becomes small enough. The rim of fluid formed during an asperity dewetting process is likely not to move fluid directly to the edges of the nominal contact region, but rather to large interfacial flow channels from where the fluid is channeled to the edges of the contact region. When the final (long contact time) contact area $A/A_0 \ll 1$ then many large flow channels will percolate and the fluid can quickly escape without building up a large fluid pressure in the flow channels. In this case the fluid removal (both squeeze-out and dewetting) will occur fast as in the first system (a) studied above. However, if $A/A_0 > 0.42$ at some point in time, the contact area will percolate, which may drastically slow down also the dewetting process as no percolating fluid flow channels will prevail at long contact times. No theory exists at present which can describe simultaneously squeeze-out and dewetting for randomly rough surfaces, but we believe that including dewetting will result in a contact area which will grow beyond the percolation limit (at $A/A_0 \approx 0.42$, see [38]), which would be the largest possible contact area in the absence of dewetting (see figure 25(c)).

Even for dewetting one would expect that the speed of fluid removal should depend on the fluid viscosity η (and on the effective interfacial binding energy $\Delta\gamma$), while we found experimentally that fluids with very different viscosities exhibit nearly the same time dependence of the friction coefficient (or the area of contact) as shown in figure 20. Stated differently, from all the parameters η, $\Delta\gamma$, E (elastic modulus), nominal pressure σ_N and the length parameters

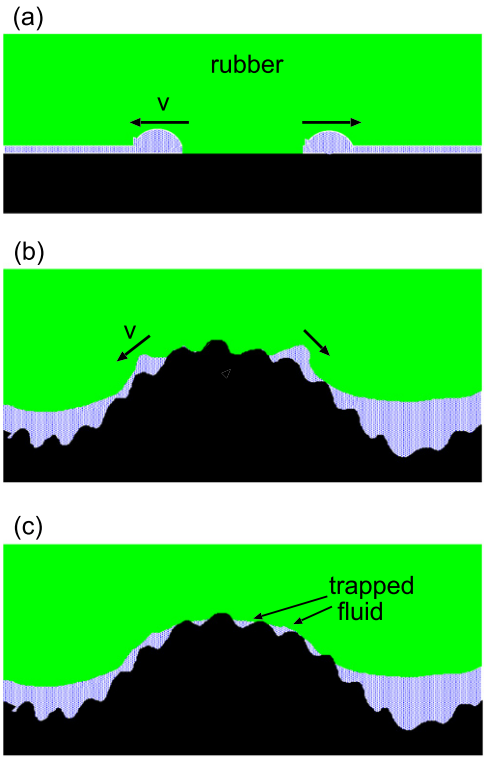

Figure 25. (a) Dewetting transition between rubber with a flat surface and a rigid substrate with a flat surface. (b) Dewetting transition starting close to the top of a substrate asperity, with a moving rim transferring fluid towards the surrounding valleys. (c) In the absence of dewetting the fluid remains trapped so that even after a long time at least ∼60% of the surface area will contain trapped (sealed-off) fluid.

involved (radius R of the ball or cylinder, and the surface roughness power spectrum $C(\mathbf{q})$, which we assume is a self-affine fractal with the Hurst exponent H and the large and small wavevector cut-off q_1 and q_0) the only way to obtain a parameter with dimension time is in the combination $(\eta/E)f[p/E, \Delta\gamma/(RE), H, Rq_0, q_1/q_0]$, i.e., the squeeze-out time in a theory which only depends on the parameters given above *must* be proportional to the fluid viscosity, contrary to what we observe. Thus, some other parameter (and new physics) must enter in the theory. This could, for example, be the viscoelastic properties of the rubber (which also could influence the speed of dewetting), a time dependence (ageing effect) of the effective interfacial binding energy $\Delta\gamma$, or a time associated with diffusion of molecules in the PDMS rubber. However, the last two effects would depend on the fluid used, and therefore seem unlikely to be relevant. Another possibility is related to the observation reported on in appendix B, where for the PDMS ribs in contact with the ground PMMA it was observed that after a very long contact time (about 2.6×10^5 s or three days) we also observed transfer of non-crosslinked PDMS chains to the substrate. The transfer of free PDMS chains to surface non-contact (or low-pressure) regions is caused by the gradient in the hydrostatic pressure, see figure B.2. The same effect may occur also during fluid squeeze-out. That is, the pressure in the fluid, say water, in the non-contact deep valleys is lower than the pressure in

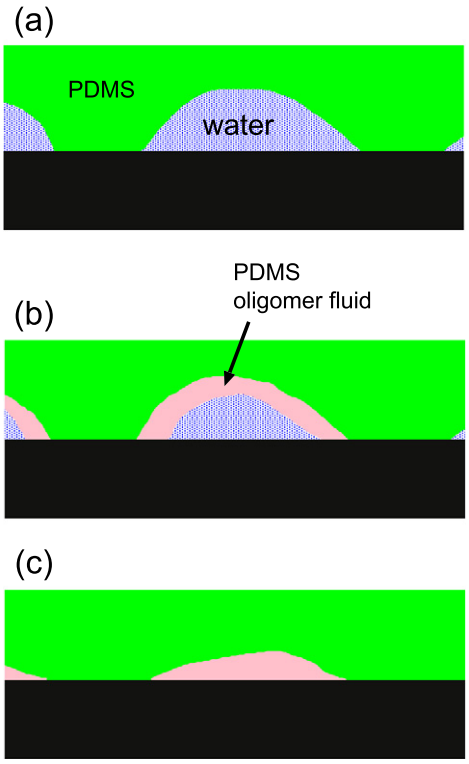

Figure 26. During fluid squeeze-out of, for example, water (blue area), non-crosslinked PDMS chains flow in the rubber to the PDMS surface, forming a thin fluid PDMS film (pink area). Finally, after removing the low viscosity (water) film the non-crosslinked PDMS chains will be removed by fluid flow, dewetting or flow back into the PDMS rubber as the PDMS fluid pressure builds up.

the asperity contact regions, and the pressure gradient (in the PDMS rubber) may result in non-crosslinked PDMS chains flowing in the rubber to the PDMS surface, forming a thin fluid PDMS film in contact with the water. At a later time the (low viscosity) water is squeezed out, resulting in the PDMS fluid in contact with the substrate, see figure 26. Finally the PDMS fluid is removed either by dewetting or by diffusion back into the silicone rubber as the pressure in the PDMS fluid filled surface areas increases. This picture would explain why the squeeze-out dynamics after long enough contact time is independent of the lubrication fluid.

To test the idea shown in figure 26 we have performed some additional breakloose friction studies for silicone rubber with the free chains extracted by swelling in a solvent (which reduce the mass of the rubber block by ≈2%). The experiments where performed against glass in a dry condition, and lubricated by water and glycerol, see figure 27. Note that the friction for silicone rubber with extracted chains is considerably higher than for silicone rubber without extracted chains, but exhibits no systematic change as a function of the time of stationary contact. On the dry substrate the friction coefficient $\mu_s \approx 1.0$ (see figure 27) while in figure 21 the breakloose friction $\mu_s \approx 0.5$. We attribute this large increase in the breakloose friction to modifications of the PDMS surface as a result of the extraction of the free chains. In water the friction is nearly as high as in the dry state, and again independent of the time of stationary contact.

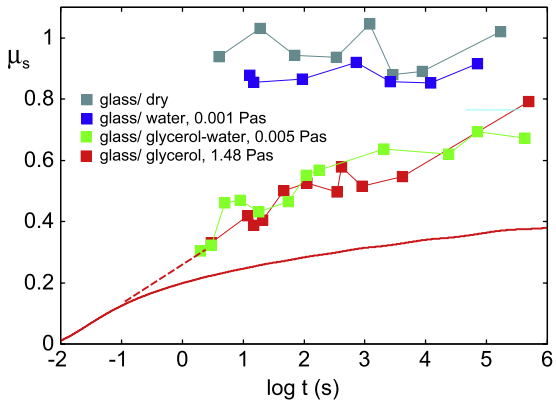

Figure 27. The breakloose friction coefficient for silicone rubber with extracted chains against glass in a dry condition, and lubricated by water, glycerol and a water–glycerol mixture.

Thus, for water, fluid squeeze-out is, as expected, fast and dewetting must occur in order for the friction to reach nearly the same value as for the dry surface. The slightly smaller friction in water may be due to some poles of trapped (sealed-off) water which may occur even when dewetting occurs. Finally, in glycerol the fluid removal is as slow as in the case of PDMS without extracted chains, i.e., the process indicated in figure 26 does not seam to occur, or it has a negligible influence on the squeeze-out process. However, remarkably, again we observe as slow a squeeze-out with the water–glycerol mixture (viscosity $\eta \approx 0.005$ Pa s) as with pure glycerol, which has ≈300 times higher viscosity. We have no definitive explanation for this puzzling observation, but we would like to suggest two different possibilities:

(a) the squeeze-out of the glycerol–water mixture may involve a phase separation at the PDMS surface where a thin (some nanometers) layer of pure (or nearly pure) glycerol may form, driven by a lowering of the interfacial energy. Thus the last step in the fluid removal (involving dewetting) may involve removing only the glycerol, even for the glycerol–water mixture. Since glycerol has a viscosity very close to that of the silicone oil used in figure 20, this could also explain the very similar squeeze-out of the water–glycerol mixture as for the silicone oil.

(b) The second possibility was suggested to us by Manoj Chauhudry. It is possible that when the soft PDMS ribs are pressed against a thin liquid coated substrate, the film breaks and the soft polymer makes contact with the substrate in such a way as to produce channels, as recently observed in a study of how a blister heals [39]. The trapped liquid flows out of these channels. A more viscous liquid will exert a larger lubrication pressure during the formation of such channels, so that its equivalent hydraulic diameter is more than for the channels produced by lower viscosity liquids. Thus there could be a compensation between large hydraulic diameter and large viscosity in the eventual squeezing out of the liquid film. The effect may become important above a certain viscosity.

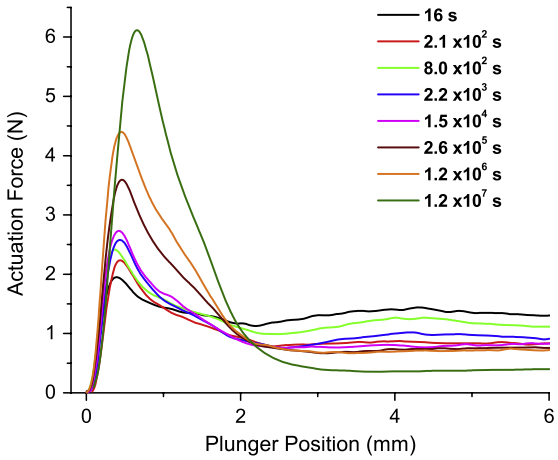

Figure 28. The force as a function of displacement of the rubber stopper for various times of stationary contact. Note that the breakloose force increases with the time of stationary contact due to squeeze-out of the high viscosity lubricant fluid (silicone oil). Note also that the kinetic friction force decreases with the time of stationary contact, which is probably due to viscoelastic relaxation of the rubber which lowers the contact pressure and changes the shape of the rubber rib contact region.

5. Application to pre-fillable syringes

Syringes are the most common pre-filled parenteral drug delivery systems, in which a rubber plunger stopper is actionated to expel the injectable liquid drug from a cylindrical glass or polymer barrel (see figure 1(c)). Low, uniform and stable gliding forces of the plunger stopper are critical for patient comfort and healthcare professional convenience in manual use of pre-fillable syringes; when syringes are used in conjunction with self-administration devices (autoinjectors) gliding performance is even more critical [40]. The plunger stopper needs to ensure also the container integrity or sealing, to ensure no drug dose changes and maintain sterility. This is particular important for pre-filled syringes where the drug can be stored in the device for several years before use. Traditionally the inner surface of the syringe is lubricated by a high viscosity silicone oil (viscosity $\eta \approx 0.35$–10 Pa s) to ensure good gliding performance. The nominal contact pressure between the ribs of the stopper and the glass barrel is a critical parameter for sealing and reaches very high values, of the order of $\sim$1 MPa. The silicone oil is squeezed out from the barrel–stopper interface very slowly because of its high viscosity. This squeeze-out causes a continuous increase of the breakloose (or static) friction before the syringe is used, as shown in figure 28. In some cases this may result in such a high breakloose force that it hinders the functionality of the device during the injection. It is therefore of great importance to understand the exact origin and nature of the breakloose friction.

In the application to syringes, the system consists of round or flat ribs in contact with the syringe's barrel surface. The contact can be described as a rectangular region of width $w \approx 1$ mm (x-direction) and of infinite length (because of the circular nature of the contact region) (y-direction).

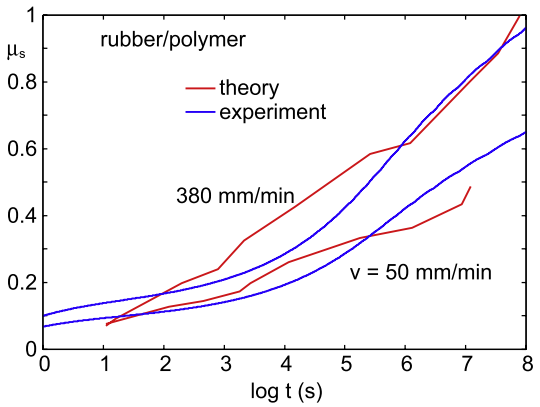

Figure 29. The static (or breakloose) friction force as a function of the logarithm of the waiting time for syringes with polymer tubes. Plastic tubes lubricated with ≈12.5 Pa s silicone oil.

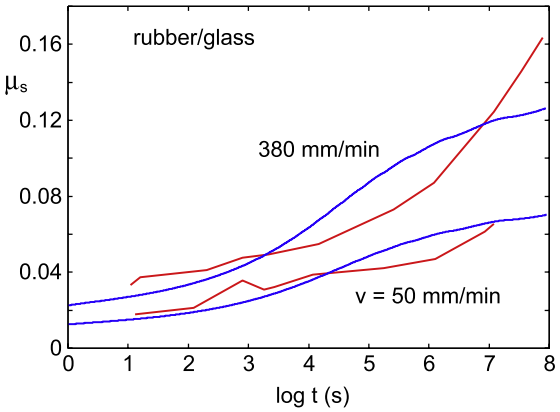

Figure 30. The static (or breakloose) friction force as a function of the logarithm of the waiting time for syringes with glass tubes. Glass tube lubricated with 1 Pa s silicone oil.

The start-up or breakloose friction will depend sensitively on the squeeze-out dynamics and in a first approximation (at least for small start-up velocities) one may assume that it is proportional to the area of real contact.

We have measured the start-up (or breakloose) friction coefficient (and the kinetic friction coefficient) as a function of the logarithm of the waiting time for syringes with inert polymer and glass barrels, see red lines in figures 29 and 30. To generate this data, syringes were empty and without the needle to avoid any pressure drop contribution from the needle. The syringe's barrel–rubber-stopper system was assembled as follows: (a) for short storage times (<100 s) the systems were assembled manually, and (b) for long storage time all systems were assembled in a vacuum placement unit. At different time points, five syringes were actionated in an automatic compression bench at fixed speed, and the forces needed to initiate and sustain the movement of the plunger were recorded.

It is interesting to note that as the time approaches zero the start-up friction values approach the kinetic friction values (not shown). This is, of course, expected because after a very short waiting time the fluid film thickness will be similar to that during injection.

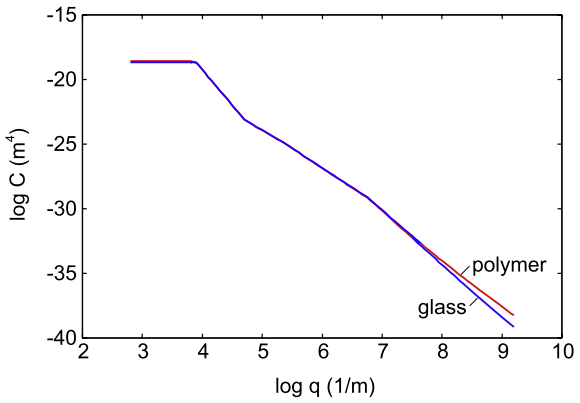

Figure 31. The combined surface roughness power spectrum of the rubber–glass and rubber–polymer systems. The power spectrum was obtained from 3D topography data of the syringe's inner and the stopper's outer surfaces. The topography was measured at long wavelengths over a 2 mm × 2 mm surface area using a 3D Stylus (Dektak XT, Bruker, Germany), at intermediate wavelength over a 23 μm × 93 μm region using an optical profilometer (Wyko 9100, Bruker, Germany), and at short wavelength over a 10 μm × 10 μm surface area using an AFM (Dimension 3100, Bruker, Germany).

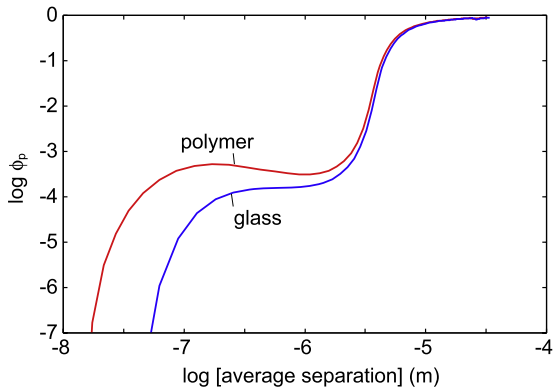

Figure 32. The fluid flow factor $\phi(\bar{u})$ as a function of the average interfacial separation $\bar{u}$ for the rubber–glass and rubber–polymer systems.

In an earlier publication we have studied the fluid squeeze-out between the rubber stopper and the glass barrel [11]. However, we have now obtained a more accurate surface roughness topography of all the surfaces involved (rubber stopper and glass and polymer barrels), and here we compare the experimental results presented above with new squeeze-out calculations. Figure 31 shows the combined surface roughness power spectra of the rubber–glass and rubber–polymer systems, as obtained from the measured surface topography. As in section 4.4, the calculation below uses the Reynolds thin film fluid flow equation for surfaces with random roughness. Using this approach one can integrate-out, or average-out, the surface roughness to obtain a new effective equation of motion for the fluid flow between smooth surfaces. This equation is similar to the Reynolds equation, but with a renormalized viscosity $\eta_{\rm eff} = \eta/\phi_{\rm p}(\bar{u})$ which depends on the local average surface separation $\bar{u}$ (which will vary with the position $\mathbf{x}$ in the xy-plane). In figure 32 we show the fluid flow factor $\phi_{\rm p}(\bar{u})$, as a function of the locally averaged interfacial separation $\bar{u}$, as calculated using the Persson contact mechanics theory in combination with the Bruggeman effective medium theory, see [36, 45]. For surface roughness with isotropic statistical properties $\phi_{\rm p} < 1$. Note that $\phi_{\rm p} \to 1$ as $\bar{u} \to \infty$, as expected because the surface roughness becomes unimportant for very large interfacial separation. Since $\eta_{\rm eff} = \eta/\phi_{\rm p}(\bar{u}) > \eta$ the surface roughness will increase the effective viscosity. In particular, as the interfacial separation decreases the area of real contact increases, and for $A/A_0 \approx 0.42$ the contact area percolates [38] and no fluid flow can occur. This limit corresponds to $\phi_{\rm p} = 0$ and $\eta_{\rm eff} = \infty$, and is the reason for the fast decrease in $\phi_{\rm p}$ for small interfacial separations $\bar{u}$ in figure 32. Note that the polymer surface has a larger roughness than the glass surface at a very short length scale (see figure 31). This will result in a smaller contact area, and a larger average interfacial separation in the apparent contact regions observed at large magnification. As a result, the pressure flow factor for small interfacial separations is larger for the polymer barrel than for the glass barrel (see figure 32). Thus, short wavelength roughness decreases the effective viscosity for small surface separations, while the long wavelength roughness, for surfaces with isotropic statistical properties, always increase the effective viscosity.

The red lines in figures 29 and 30 show the measured static (or breakloose) friction coefficient (obtained by dividing the measured breakloose friction force by the normal force $F_{\rm N} = 52$ N) as a function of the logarithm of the waiting time for syringes with glass and polymer barrels, and for the driving velocities $v \approx 6$ and ≈ 0.8 mm s^{-1}. Assuming that the friction force is proportional to the contact area A, we can write (see (1)):

$$\tau_{\rm s} = \mu_{\rm s}\sigma_{\rm N}(A_0/A)$$

where $\tau_{\rm s}$ is the breakloose frictional shear stress in the area of real contact. The nominal contact area is estimated as $A_0 = 3 \times 2\pi Rw$, where $R \approx 3.18$ mm is the radius and $w \approx 1$ mm the width of the nominal rubber–glass (circular) contact region. Thus, $A_0 \approx 6 \times 10^{-5}$ m^2. The blue lines in figure 30 show the calculated breakloose friction coefficient assuming the rubber–glass breakloose frictional stress $\tau_{\rm s} \approx 0.30$ MPa at $v = 6$ mm s^{-1} and $\tau_{\rm s} \approx 0.17$ MPa at $v \approx 0.8$ mm s^{-1}. For the polymer barrel (see figure 29) the frictional shear stresses are much higher, namely $\tau_{\rm s} \approx 2.5$ MPa at $v = 6$ mm s^{-1} and $\tau_{\rm s} \approx 1.7$ MPa at $v \approx 0.8$ mm s^{-1}.

In the calculations above we have used the surface roughness power spectra for the combined surfaces of the rubber–glass and rubber–polymer systems, see figure 31. Note that the combined power spectra differs only for large wavevectors, but this fact, and the difference in the viscosity of the silicone oil used, explain the rather large difference in the squeeze-out dynamics (see figure 33 for the time dependence of the area of contact).

In the present application the area of real contact is always below the percolation limit (at $A/A_0 \approx 0.42$). This is shown in figure 33 for both the rubber–glass and

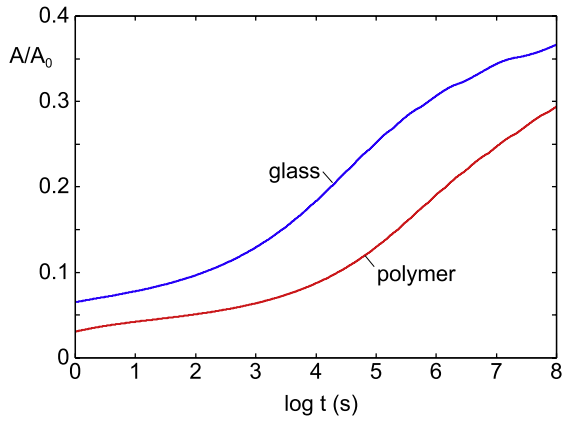

Figure 33. The area of real contact for the glass and polymer barrel.

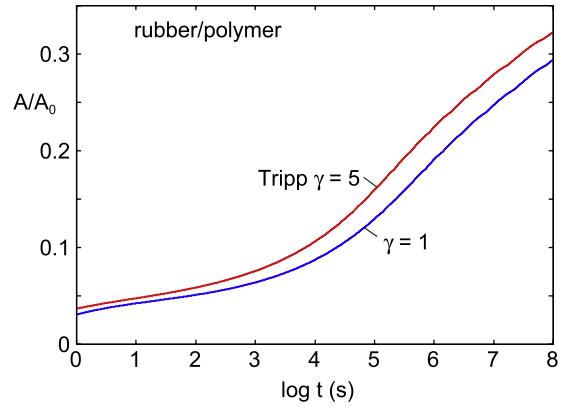

Figure 34. The area of real contact for the polymer barrel for the Tripp number $\gamma = 1$ and $\gamma = 5$.

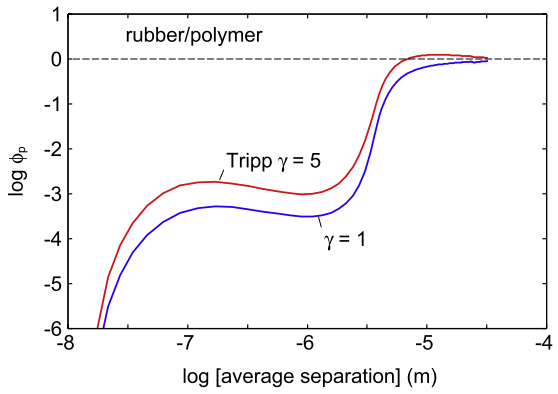

Figure 35. The fluid flow factor $\phi(\bar{u})$ as a function of the average interfacial separation $\bar{u}$ for the rubber–polymer systems with isotropic combined surface roughness ($\gamma = 1$) and for anisotropic roughness ($\gamma = 5$) with the 'grooves' along the fluid squeeze-out direction.

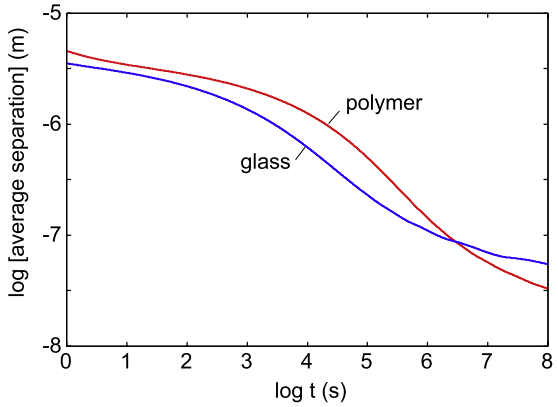

Figure 36. The average surface separation as a function of the time of stationary contact.

rubber–polymer contacts. Thus we attribute the time dependence of the breakloose friction mainly to the (Reynolds) hydrodynamic squeeze-out dynamics, even though dewetting may occur in the asperity contact regions. For very large times (not shown) the contact area will probably continue to increase beyond the percolation limit (as found in section 4), but this is of no practical importance in the present case, and cannot be studied experimentally (the present experimental data already involved up to 907 days waiting time). In some medical applications, such as disposable empty syringes, a shelf life of 4–5 years (about 1825 days or 1.5×10^8 s) may be applicable, but in most cases the syringes are used within the tested 2.5 years.

The polymer barrel has anisotropic roughness but in figure 34 we show that even for a relative large asymmetry (defined by the Tripp number γ) there is relatively small change in the time dependence of the contact area. Note that for anisotropic roughness, with the 'grooves' along the fluid squeeze-out direction (corresponding to $\gamma > 1$), squeeze-out is, as expected, faster than for surface roughness with isotropic properties. This also manifests itself in a region for larger surface separation where the fluid pressure flow factor $\phi_p > 1$, see red line in figure 35. That is, for large enough interfacial separation the roughness (channels along the fluid flow direction) facilitates the removal of the fluid, and the effective viscosity $\eta_{eff} = \eta/\phi_p$ is then smaller than the bar viscosity η. (For anisotropic roughness the pressure flow factor ϕ_p and the effective viscosity η_{eff} are actually 2D tensors, and the fluid flow driven by a pressure gradient orthogonal to the channels is smaller than for isotropic roughness.) However, for shorter surface separation $\phi_p < 1$ and when the contact area percolates $\phi_p = 0$, corresponding to an infinite effective viscosity.

In the study above we have neglected the contribution to the friction from shearing the silicone oil film in the non-contact region. We will now show that this is a good approximation. In figure 36 we show the average surface separation as a function of the time of stationary contact for both the glass and polymer barrel. At the longest time the average separation is $\bar{u} \approx 20$ nm for the polymer and $\bar{u} \approx 60$ nm for the glass barrel. Since at this time the relative area of real contact is of the order of ≈0.35, the average surface separation in the non-contact region is ≈30 nm and ≈90 nm, respectively. A fluid film with thickness d sheared with the velocity v will give rise to a frictional shear stress $\tau = \eta v/d$. However, in the present case the shear rate $\dot{\gamma} = v/d$ is so large that shear thinning occurs for the polymer barrel case. For silicone oil to a good approximation $\eta = \eta_0/[1 + (\eta_0/B)\dot{\gamma}^n]$.

If the bulk viscosity η_0 is measured in Pa s and the shear rate in 1 s^{-1} we have $B \approx 8 \times 10^4$ and $n \approx 0.9$. With $v = 1$ mm s^{-1} we get $\dot{\gamma} \approx 3 \times 10^4$ s^{-1} and $\dot{\gamma} \approx 1 \times 10^4$ s^{-1} for the polymer and glass barrels, respectively. Thus for the polymer barrel (with $\eta_0 = 12.5$ Pa s) $\eta \approx 5$ Pa s while for the glass barrel negligible shear thinning occurs for the film thickness 90 nm. Using $\tau = \eta v/d$, for the velocity $v = 1$ mm s^{-1}, this gives the frictional shear stresses 0.17 MPa and 0.01 MPa for the 30 nm and 90 nm thick silicone oil films, respectively. These values should be compared with the frictional shear stress acting in the area of real contact (at $v \approx 0.8$ mm s^{-1}), which we found above to be ≈1.7 MPa and ≈0.17 MPa, respectively. Since the area of real contact is only about half of the non-contact area one needs to divide the latter values by a factor of two when comparing the relative contributions from the contact and non-contact area to the nominal frictional shear stress. Thus, this rough estimate indicates that at the lowest breakloose sliding speed ($v \approx 0.8$ mm s^{-1}) the contribution to the nominal frictional shear stress from the non-contact area will be of the order of 17% for the polymer barrel and 11% for the glass barrel. Because of the shear thinning, for the higher velocity ≈6 mm s^{-1}, we get for the polymer barrel $\eta \approx 1.2$ Pa s and for the glass barrel $\eta \approx 0.78$ Pa s. Using these values gives (for $v = 6$ mm s^{-1}) the frictional shear stresses 0.24 MPa and 0.052 MPa, respectively. These values should be compared with the shear stresses acting in the area of real contact in this case, namely (see above) ≈2.5 MPa and ≈0.30 MPa. Thus, this rough estimate indicates that, at the $v = 6$ mm s^{-1} breakloose sliding speed, the contribution to the nominal frictional shear stress from the non-contact area may be of the order of 16% for the polymer barrel and 25% for the glass barrel.

We have found above that for the bromobutyl rubber stopper in contact with the glass barrel the frictional shear stress in the area of contact is very similar to that of PDMS in contact with glass. However, when the same stopper is used in the polymer barrel the calculated frictional shear stress in the area of real contact is about ≈10 times higher. This indicates that there is a stronger adhesive interaction and pinning of the rubber molecules when in contact with the polymer, as compared to the glass surface. This is consistent with the following observation: we have studied the width of the rib–barrel interface with an optical microscope as a function of the time of stationary contact. For the rubber–glass system there is a negligible increase in the width of the rib contact regions, namely an ≈1.2% increase for the first rib (from 0.892 to 0.903 mm after 907 days of contact), while no increase in the width is observed for the second and third rib. However, for the rubber–polymer system the width of the rib–polymer contact regions increases by 13.7%, 8.5% and 4.4% for the first, second and the third rib, respectively, after 907 days of contact. This indicates that an adhesive rubber–polymer interaction develops as the contact time increases, and we believe that this is also the origin of the much higher frictional shear stress for the rubber–polymer system.

In the experiments it was also observed that the sustaining or kinetic friction forces decreased continuously with the time of stationary contact, which we attribute to viscoelastic relaxations in the rubber reducing the contact pressure. This 'softening' of the rubber with increasing time will also influence the time-evolution of the area of real contact, but was found to be negligible for PDMS rubber. Using pressure sensitive paper we measured (for both the glass and polymer barrel) a change in the contact pressure due to viscoelastic relaxations from the average pressure 0.87 ± 0.3 MPa to 0.6 ± 0.1 MPa after 907 days of contact.

A more complete analysis of the problem studied above requires accurate information about how the frictional shear stress (for dry surfaces) depends on the time of stationary contact. For bromobutyl rubber in contact with the polymer this may involve the formation of stronger interfacial bonds than for the (very inert) PDMS. One complication is that the applied tangential force will compress the rubber stopper, which in turn will increase the normal stress the rubber ribs exert on the barrel. An accurate estimate of this effect may require detailed FEM calculations or experimental measurements.

6. Summary and conclusion

We have presented experimental data for the static or breakloose friction for lubricated elastomer contacts, as a function of the time of stationary contact. Due to fluid squeeze-out from the asperity contact regions, the breakloose friction force increases continuously with the time of stationary contact. When the final (long contact time) contact area $A/A_0 \ll 1$, as is the case if the surface roughness is high enough and the nominal contact pressure small enough (as in the first system (a) studied above), then many large flow channels will percolate and the fluid can quickly escape without building up a large fluid pressure in the flow channels. In this case the fluid removal (both squeeze-out and dewetting) will occur fast. However, if $A/A_0 > 0.42$ at some point in time, as observed if the surfaces are smooth enough and the nominal contact pressure large enough (as for the second system (b) studied above), the contact area will percolate, which may drastically slow down also the dewetting process as no percolating fluid flow channels will prevail at long contact times. No theory exists at present which can describe simultaneously squeeze-out and dewetting for randomly rough surfaces, but we believe that including dewetting will result in a contact area which will grow beyond the percolation limit. However, remarkably, different fluids with very different viscosities, ranging from 0.005 Pa s (water–glycerol mixture) to 1.48 Pa s (glycerol), give very similar breakloose friction forces as a function of the time of stationary contact. The increase in the breakloose friction is mainly due to the increase in the area of real contact with increasing contact time due to fluid squeeze-out and dewetting, but may involve additional physical processes in order to explain the similar squeeze-out times for fluids with very different viscosities.

Acknowledgments

We thank A Chateauminois and M Chaudhury for interesting discussions. We thank C Fuentes (BD France) for help with the surface topography measurements.

Appendix A. Additional comments on fluid squeeze-out

The most surprising result presented above is that the breakloose friction for several different lubrication fluids, with very different viscosities, exhibit nearly the same increase with the time of stationary contact. We have argued that most likely dewetting transitions take place on all surfaces, resulting in dry asperity contact regions. However, even if a thin (nanometer) film of lubricant molecules remained in the contact regions one expects a similar frictional shear stress $\tau_s \approx 0.4$ MPa as found above after a long contact time. Thus, experimental studies [42] and theory [43] have shown a nearly universal behavior of the effective viscosity of nanometer thin confined films at normal pressures of the order of ~1 MPa, as prevailing in the present case. Thus the experimental study presented in [42] gives $\eta_{\rm eff} = B\dot\gamma^{-n}$ (where $\dot\gamma = v/d$ is the shear rate) with $B \approx 10^5$ Pa s and $n \approx 0.9$ (assuming that $\dot\gamma$ is measured in SI units). In the present case $v \approx 1$ mm s^{-1} and with $d \approx 10^{-9}$ m we get $\tau_s = \eta_{\rm eff}\dot\gamma = B\dot\gamma^{1-n} \approx 0.4$ MPa.

Consider a rigid rectangular block of width w and length $L \gg w$ squeezed against a flat rigid substrate surface in a viscous fluid. Assume that all surfaces are perfectly smooth. For rigid solids with flat parallel surfaces no dewetting transition can occur. In this case, if $h(t)$ is the separation between the surfaces at time t and $h(0) = h_0$ at time $t = 0$ then

$$\frac{1}{h^2(t)} - \frac{1}{h_0^2} = \frac{2p_0 t}{\eta w^2}$$

where $p_0 = F_N/(wL)$ is the nominal squeezing pressure and η the fluid viscosity. Thus, after long enough time $h(t)/h_0 \ll 1$ we get

$$h(t) \approx \left(\frac{\eta w^2}{2p_0 t}\right)^{1/2}. \tag{A.1}$$

If the surfaces after the squeeze-time t_0 are moved laterally we get the frictional shear stress

$$\tau_s \approx \frac{\eta v}{h(t_0)} = (2p_0 t_0 \eta)^{1/2}\frac{v}{w}. \tag{A.2}$$

Thus, in this idealized case one would expect the start-up friction force to *increase* with the viscosity η of the fluid.

Even for perfectly flat and parallel surfaces, (A.2) is only valid as long as the film thickness is larger than a few nm. For smaller film thicknesses the lubrication film starts to behave more like a solid than a fluid, with a nearly universal shear stress τ_s as discussed above. Now the time t_1 it takes for the film thickness to decrease to $h = h_1$ is given by

$$t_1 \approx \frac{\eta w^2}{2p_0 h_1^2} \tag{A.3}$$

and decreases as the viscosity decreases. Thus, according to this picture the breakloose friction will reach its maximum value faster for a low viscosity fluid. In fact, the time it takes for the friction to reach the saturation limit according to (A.3) is proportional to the fluid viscosity η, which is also what is obtained in the full elastohydrodynamic calculations (not shown).

According to (A.3) it would take $t_1 \approx 2.7 \times 10^5$ s for the film thickness to reach $h_1 \approx 1$ nm, assuming the width $w = 0.4$ mm, the viscosity $\eta = 1$ Pa s and the nominal pressure $p_0 = 0.3$ MPa. In reality the surfaces have surface roughness and only asperity contact occurs. In the present case (without dewetting) the area of contact has reached half of its final (asymptotic long time) value after about 100 s (see figure 17). However, in the present case the final asymptotic contact area is not reached even after $t \approx 10^6$ s (see figure 17). The reason is that because the surfaces in the present case are relatively smooth, the contact area on the dry surface is higher than at the point where the contact area percolates (at $A = A_c \approx 0.42A_0$). (In the present study we have used the effective medium theory to calculate the pressure flow factor ϕ_p which enters in the equation for fluid squeeze-out. The original Bruggeman theory gives $A_c/A_0 = 0.5$, see [11, 13, 44, 45], but we have modified the theory as described in [38] to give the correct percolation limit.) Thus after a long time, in the absence of dewetting, when the contact area is close to the percolation limit A_c, fluid regions will be sealed-off at the interface, and the fluid squeeze-out will occur only through very narrow flow channels, which is a slow process due to the viscous dissipation. This is the reason why, even after $t \approx 10^6$ s, the contact area still continues to increase with the time of stationary contact (see figure 17). If the surfaces were rougher, or the nominal contact pressure smaller, the contact area would be smaller than A_c (percolation limit) and the contact area would approach its final value much faster than in the present case (see figure 17) [9, 10]. This is also observed in figure 22, where for the ground (roughened) PMMA surfaces the squeeze-out occurs much faster, in particular when the wear channels are along the fluid squeeze-out direction. As discussed in section 3.3, we believe that in the present case dewetting occurs. In this case the contact area is not limited to a value below $A = A_c \approx 0.42A_0$, but can increase towards complete contact if the applied pressure and the effective interfacial binding energy ($\Delta\gamma = \gamma_{RL} + \gamma_{LS} - \gamma_{RS}$, R = rubber, S = substrate, L = liquid) are large enough.

Appendix B. Weeping lubrication

For the PDMS ribs in contact with the ground PMMA it was observed that after a very long contact time (about 2.6×10^5 s or three days) the breakloose friction was considerable lower ($\mu_s \approx 0.63$) than what is shown in figure 13. In this case we also observed transfer of non-crosslinked PDMS chains to the substrate. The transferred PDMS can be seen as slightly darkened strips on the PMMA substrate in figure B.1, to the right of the rubber block (which was moved to a new position). The transfer of free PDMS chains to surface non-contact

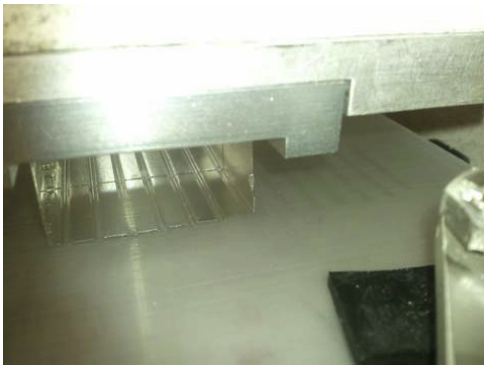

Figure B.1. The slightly darkened strips on the PMMA substrate to the right of the rubber block are due to transfer of PDMS chains to the PMMA after three days of contact.

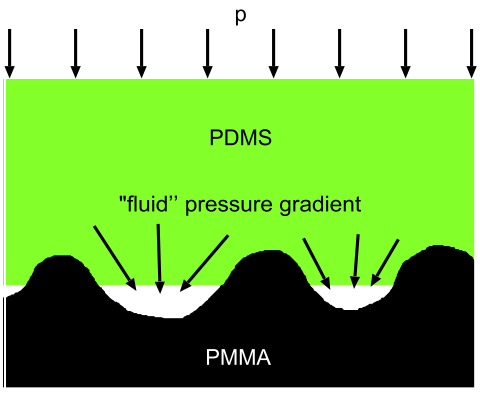

Figure B.2. The gradient in the hydrostatic pressure drives free PDMS chains ('fluid') into the non-contact (or low-pressure) regions at the interface.

(or low-pressure) regions is caused by the gradient in the hydrostatic pressure, see figure B.2. It is interesting to note that when the block was first removed and then put back on the track containing the PDMS fluid, the breakloose friction even after a short contact time showed a reduced value ($\mu_s \approx 0.69$), only slightly larger than after the long (three day) contact time. This shows that the reduction in the friction is due to the lubrication action by the PDMS fluid, and is similar to the mechanical squeeze-out of the synovial fluid held in the porous cartilage (so-called weeping lubrication), (see footnote 2).

Appendix C. Viscoelastic contribution to PDMS friction

In this appendix we calculate the contribution to the friction coefficient from the viscoelastic energy dissipation in PDMS induced by the pulsating deformations of the rubber surface by the substrate asperities. PDMS is usually considered as a nearly perfect elastic material, but this is only true for low-frequency deformations and high enough temperatures. Here we will calculate the PDMS rubber friction on the ground PMMA surface.

The red and green lines in figure C.1 show the 2D-power spectra for a surface with isotropic roughness, with the

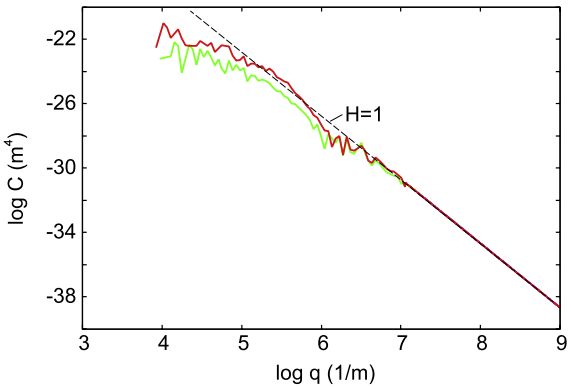

Figure C.1. The red and green lines are the 2D-power spectra for a surface with isotropic roughness, with the 1D-power spectra given in figure 10 by the red and green lines. The ground PMMA surface is anisotropic, but using the two power spectra in this figure will give an upper and lower bound for the calculated friction on the actual anisotropic surface. The measured data has been extrapolated linearly (on the log–log scale) to larger wavevectors. The slope of the extrapolation line corresponds to a self-affine fractal surface with the Hurst exponent $H = 1$. The red curve corresponds to a surface with an rms roughness $h_{\rm rms} = 1.33$ μm and an rms slope $\xi = 0.32$. The green curve corresponds to a surface with an rms roughness $h_{\rm rms} = 0.42$ μm and an rms slope $\xi = 0.28$.

1D-power spectrum given in figure 10 by the red and green lines. The ground PMMA surface is anisotropic, but using the two power spectra given in this figure will give an upper and lower bound for the friction on the actual anisotropic surface. The measured data has been extrapolated linearly (on the log–log scale) to larger wavevectors. The slopes of the extrapolation lines correspond to a self-affine fractal surface with the Hurst exponent $H = 1$. The red curve corresponds to a surface with an rms roughness $h_{\rm rms} = 1.33$ μm and an rms slope $\xi = 0.32$. The green curve corresponds to a surface with an rms roughness $h_{\rm rms} = 0.42$ μm and an rms slope $\xi = 0.28$. Figure C.2 shows (a) the real and imaginary part of the viscoelastic modulus, and (b) $\tan\delta$ for PDMS as a function of frequency at room temperature $T = 20\,^{\circ}$C.

Figure C.3 shows the contribution to the friction coefficient from the viscoelastic energy dissipation in PDMS induced by the pulsating deformations of the rubber by the substrate asperities. Also shown is the relative contact area A/A_0 as a function of the logarithm of the sliding velocity v. In the calculation we have used the measured PDMS viscoelastic modulus from figure C.2 and the angular averaged surface roughness power spectrum given in figure C.1. The temperature $T = 20\,^{\circ}$C and the nominal pressure $p_0 = 0.3$ MPa.

Figure C.4 shows the cumulative friction coefficient as roughness with increasing wavevectors is included in the calculation. For the same system as in figure C.3 at the sliding velocity $v = 1$ m s^{-1}. Note that the surface roughness components for each decade in wavevector are roughly equally important.

We have not measured the surface roughness power spectrum of the ground PMMA surface for wavevectors larger than $\approx 10^7$ m^{-1}. To test how sensitive the friction coefficient

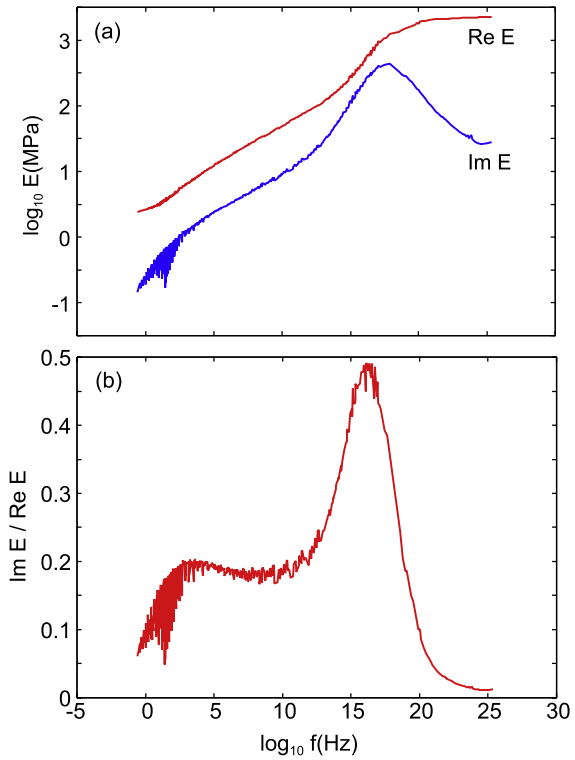

Figure C.2. (a) The real and imaginary part of the low-strain viscoelastic modulus, and (b) tan δ for PDMS as a function of frequency at room temperature $T = 20\,^{\circ}\mathrm{C}$ (adapted from [13]).

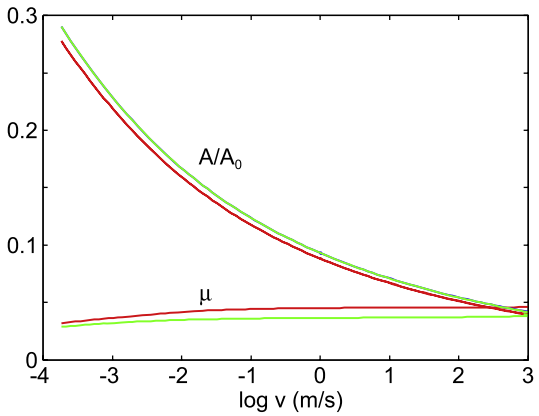

Figure C.3. The contribution to the friction coefficient from the viscoelastic energy dissipation in PDMS induced by the pulsating deformations of the rubber surface by the substrate asperities. Also shown is the relative contact area A/A_0 as a function of the logarithm of the sliding velocity v. For $T = 20\,^{\circ}\mathrm{C}$ and the nominal pressure $p_0 = 0.3$ MPa. In the calculation we have used the measured PDMS viscoelastic modulus from figure C.2 and the angular averaged surface roughness power spectrum given in figure C.1.

is to the (extrapolated) large wavevector region we have calculated the rubber friction using the power spectrum shown in figure C.5. The red line in figure C.5 is the 2D-power spectrum for a surface with isotropic roughness, with the 1D-power spectrum given in figure 10 by the red line, and the extrapolation used above. The slope of the extrapolation

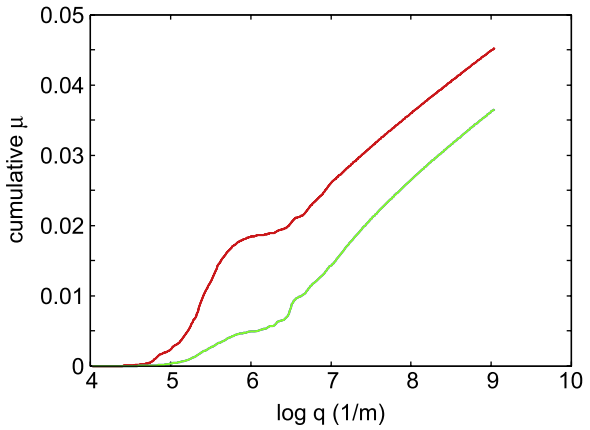

Figure C.4. The cumulative friction coefficient as roughness with increasing wavevectors is included in the calculation. For the same system as in figure C.3 at the sliding velocity $v = 1$ m s^{-1}.

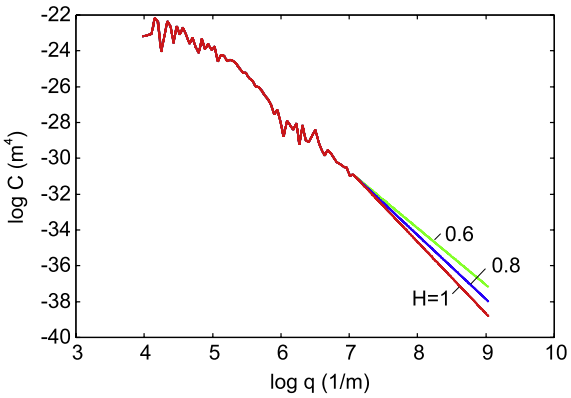

Figure C.5. The red line is the 2D-power spectrum for a surface with isotropic roughness, with the 1D-power spectrum given in figure 10 by the red line. The slope of the extrapolation lines corresponds to a self-affine fractal surface with the Hurst exponent $H = 1$ (red), 0.8 (blue) and 0.6 (green). The red curve corresponds to a surface with an rms roughness $h_{\mathrm{rms}} = 0.42$ μm and an rms slope $\xi = 0.28$. The green curve corresponds to a surface with an rms roughness $h_{\mathrm{rms}} = 0.46$ μm and an rms slope $\xi = 0.85$.

lines corresponds to a self-affine fractal surface with the Hurst exponent $H = 1$ (red), 0.8 (blue) and 0.6 (green). The red curve corresponds to a surface with an rms roughness $h_{\mathrm{rms}} = 0.42$ μm and an rms slope $\xi = 0.28$. The green curve corresponds to a surface with an rms roughness $h_{\mathrm{rms}} = 0.46$ μm and an rms slope $\xi = 0.85$.

Figure C.6 shows the contribution to the friction coefficient from the viscoelastic energy dissipation in PDMS induced by the pulsating deformations of the rubber surface by the substrate asperities, as a function of the logarithm of the sliding velocity v. For $T = 20\,^{\circ}\mathrm{C}$ and the nominal pressure $p_0 = 0.3$ MPa. In the calculation we have used the measured PDMS viscoelastic modulus from figure C.2 and the angular averaged surface roughness power spectra given in figure C.5.

Finally, figure C.7 shows the cumulative friction coefficient as roughness with increasing wavevectors is included in the calculation. For the same system as in figure C.6 at a sliding velocity $v = 1$ m s^{-1}. Even using the most rough surface with the $H = 0.6$ extrapolation, gives a

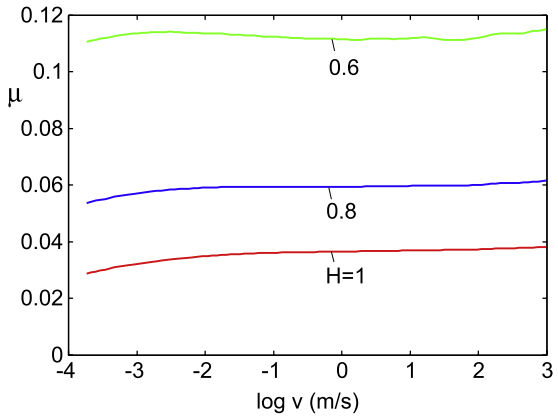

Figure C.6. The contribution to the friction coefficient from the viscoelastic energy dissipation in PDMS induced by the pulsating deformations of the rubber by the substrate asperities, as a function of the logarithm of the sliding velocity v. For $T = 20\,^{\circ}\mathrm{C}$ and the nominal pressure $p_0 = 0.3$ MPa. In the calculation we have used the measured PDMS viscoelastic modulus from figure C.2, and the angular averaged surface roughness power spectra given in figure C.5 extrapolated to larger wavevectors as indicated in the figure (curves denoted by $H = 1$, 0.8 and 0.6).

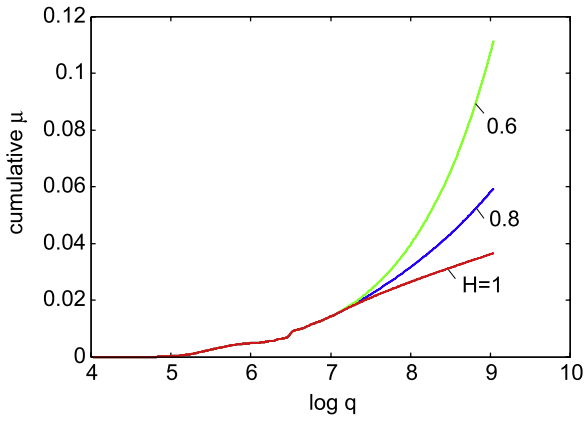

Figure C.7. The cumulative friction coefficient as roughness with increasing wavevectors is included in the calculation. For the same system as in figure C.6 at the sliding velocity $v = 1$ m s^{-1}.

rather small contribution to the observed friction. Most real surfaces have power spectra with a larger Hurst exponent than 0.6 and we conclude that the surface roughness on the ground PMMA surface gives only a small viscoelastic contribution to the observed friction.

References

[1] Persson B N J 2000 *Sliding Friction: Physical Principles and Applications* 2nd edn (Heidelberg: Springer)
[2] Dieterich J H and Kilgore B D 1994 *Pure Appl. Geophys.* **143** 283
[3] Persson B N J, Albohr O, Mancosu F, Peveri V, Samoilov V N and Sivebaek I M 2003 *Wear* **254** 835
[4] Varenberg M and Gorb S 2007 *J. R. Soc. Interface* **4** 721
[5] Varenberg M and Gorb S 2009 *Adv. Mater.* **21** 483
[6] Murarash B, Itovich Y and Varenberg M 2011 *Soft Matter* **7** 5553
[7] Lorenz B and Persson B N J 2012 *J. Phys.: Condens. Matter* **24** 225008
[8] Ben-David O and Fineberg J 2011 *Phys. Rev. Lett.* **106** 254301
[9] Lorenz B and Persson B N J 2010 *Eur. J. Phys.* E **32** 281
[10] Lorenz B and Persson B N J 2011 *J. Phys.: Condens. Matter* **23** 355005
[11] Persson B N J, Prodanov N, Krick B A, Rodriguez N, Mulakaluri N, Sawyer W G and Mangiagalli P 2012 *Eur. Phys. J.* E **35** 5
[12] Krick B A, Rodriguez N, Vail J R, Persson B N J and Sawyer W G 2012 *Tribol. Lett.* **45** 185
[13] Lorenz B, Krick B, Mulakauri N, Smolyakova M, Persson B N J and Sawyer W G 2013 *J. Phys.: Condens. Matter* **25** 225004
[14] Persson B N J and Scaraggi M 2009 *J. Phys.: Condens. Matter* **21** 185002
[15] Persson B N J 2002 *Eur. Phys. J.* E **8** 385
[16] Persson B N J, Sivebaek I M, Samoilov V N, Zhao K, Volokitin A I and Zhang Z 2008 *J. Phys.: Condens. Matter* **20** 395006
[17] Wu-Bavouzet F, Clain-Burekbuchler J, Buguin A, De Gennes P-G and Brochard-Wyart F 2007 *J. Adhes.* **83** 761
[18] Scaraggi M and Persson B N J 2012 *Tribol. Lett.* **47** 409
[19] Brochard-Wyart F and de Gennes P G 1994 *J. Phys.: Condens. Matter* **6** A9
[20] Persson B N J, Volokitin A I and Tosatti E 2003 *Eur. Phys. J.* E **11** 409
[21] Martin P and Brochard-Wyart F 1998 *Phys. Rev. Lett.* **80** 3296
Zilberman S, Persson B N J, Nitzan A, Mugele F and Salmeron M 2001 *Phys. Rev.* B **63** 055103
Roberts A D 1974 *The Physics of Tire Friction: Theory and Experiment* ed D F Hays and A L Browne (New York: Plenum)
[22] Verneuil E, Clain J, Burguin A and Brochard-Wyart F 2003 *Eur. Phys. J.* E **10** 345
[23] Carbone G, Lorenz B, Persson B N J and Wohlers A 2009 *Eur. J. Phys.* E **29** 275
[24] Chateauminois A and Fretigny C 2008 *Eur. Phys. J.* E **27** 221
[25] Schallamach A 1963 *Wear* **6** 375
[26] Chernyak Y B and Leonov A I 1986 *Wear* **108** 105
[27] Filippov E, Klafter J and Urbakh M 2004 *Phys. Rev. Lett.* **92** 135503
[28] Persson B N J and Volokitin A I 2006 *Eur. Phys. J.* E **21** 69
[29] Vorvolakos K and Chaudhury M K 2003 *Langmuir* **19** 6778
[30] Brochard-Wyart F and De Gennes P-G 2007 *Eur. J. Phys.* E **23** 439
[31] Chateauminois A, Fretigny C and Olanier L 2010 *Phys. Rev.* E **81** 026106
[32] Audry M C, Fretigny C, Chateauminois A, Teissere J and Barthel E 2012 *Eur. Phys. J.* E **35** 83
[33] Mindlin R 1949 *Trans. ASME, J. Appl. Mech.* **16** 259
[34] Johnson K L 1955 *Proc. R. Soc.* A **230** 531
[35] Bureau L, Caroli C and Baumberger T 2003 *Proc. R. Soc.* A **459** 2787
[36] Persson B N J and Scaraggi M 2011 *Eur. J. Phys.* E **34** 113
[37] Kwan M K, Lai W M and Mow V C 1984 *Ann. Biomed. Eng.* **12** 537
[38] Dapp W B, Lücke A, Persson B N J and Müser M H 2012 *Phys. Rev. Lett.* **108** 244301
[39] Longley J E, Mahadevan L and Chaudhury M K 2013 *How a Blister Heals* at press
[40] Rathore N, Pranay P, Eu B, Ji W and Wallis E 2011 *PDA J. Pharm. Sci. Technol.* **65** 468
[41] Persson B N J and Mugele F 2004 *J. Phys.: Condens. Matter* **16** R295
[42] Yamada S 2002 *Tribol. Lett.* **13** 167
see also Bureau L 2010 *Phys. Rev. Lett.* **104** 218302
[43] Sivebaek I M, Samoilov V N and Persson B N J 2012 *Phys. Rev. Lett.* **108** 036102
[44] Lorenz B and Persson B N J 2010 *Eur. Phys. J.* E **31** 159
[45] Persson B N J 2010 *J. Phys.: Condens. Matter* **22** 265004